



HAL
open science

Estimation of Elastic Strain by Integrated Image Correlation on Electron Diffraction Patterns

Qiwei Shi, Stéphane Roux, Félix Latourte, François Hild

► **To cite this version:**

Qiwei Shi, Stéphane Roux, Félix Latourte, François Hild. Estimation of Elastic Strain by Integrated Image Correlation on Electron Diffraction Patterns. *Ultramicroscopy*, 2019, 199, pp.16-33. 10.1016/j.ultramic.2019.02.001 . hal-02010262

HAL Id: hal-02010262

<https://hal.science/hal-02010262v1>

Submitted on 7 Feb 2019

HAL is a multi-disciplinary open access archive for the deposit and dissemination of scientific research documents, whether they are published or not. The documents may come from teaching and research institutions in France or abroad, or from public or private research centers.

L'archive ouverte pluridisciplinaire **HAL**, est destinée au dépôt et à la diffusion de documents scientifiques de niveau recherche, publiés ou non, émanant des établissements d'enseignement et de recherche français ou étrangers, des laboratoires publics ou privés.

Estimation of Elastic Strain by Integrated Image Correlation on Electron Diffraction Patterns

Qiwei Shi^{1,2}, Stéphane Roux¹, Félix Latourte², François Hild¹

1: Laboratoire de Mécanique et Technologie (LMT)

ENS Paris-Saclay/CNRS/Université Paris-Saclay

61 avenue du Président Wilson, 94235 Cachan, France

2: EDF R&D, Site des Renardières, avenue des Renardières

Ecuelles, 77818 Moret-sur-Loing, France

Received: date / Accepted: date

Abstract

High-angular-resolution electron backscattered diffraction (HR-EBSD) has been developed to study local elastic strains in crystals. An *integrated* Digital Image Correlation (DIC) procedure for high resolution diffraction patterns, as recently proposed to bypass several problems of the conventional cross-correlation-based algorithm, was implemented. Through two examples of experimental data where the algorithm was used and compared to conventional means, the current paper illustrates the benefits of the integrated DIC method. It is found that both measurement uncertainty and computation time were simultaneously reduced. Moreover, an enhanced robustness was obtained for relatively high misorientations relative to methods based on cross-correlation. Different computing conditions are explored on experimental data. A number of practical usage conditions are proposed to achieve better precision and speed.

Keyword: Residual stress, Integrated digital image correlation, Crystal material strain, High-angular-resolution EBSD, Deformation gradient tensor.

1 Introduction

Electron diffraction is commonly used to obtain crystallographic orientation figures in scanning electron microscopes (EBSD technique). This technique, designated herein as standard EBSD, aims principally at obtaining orientation maps with an angular resolution of the order of 0.5° . This type of uncertainty, which is mainly related to the use of the Hough transform, the accuracy of positioning the projection center (PC) and the adjustment of an undeformed lattice cell [1, 2], is sufficient to evaluate local orientations but not for elastic strain measurements, which are associated with low deformations of diffraction images. The accuracy of crystal rotation measurement by *quaternion correlation* on a series of EBSD images is also limited by crystallographic indexing [3].

The number of pixels of the detector for diffracted electrons should be increased substantially, whose effect is analyzed in Refs. [4, 5], and the analysis method improved, *i.e.*, by Digital Image Correlation (DIC), to obtain crystallographic orientations with higher accuracy [6, 7]. The proposed technique is known by the acronym HR-EBSD (for High Resolution EBSD) or HAR-EBSD (for High Angular Resolution EBSD). It has been shown that, by registering diffraction images with high resolution camera accuracy, HR-EBSD enables the elastic strains to be measured with acceptable uncertainties and excellent spatial resolution [8]. The HR-EBSD technique aims at extracting the deformation gradient tensor by comparing a reference EBSD pattern and another one corresponding to a deformed state. The technique processes diffraction images of good resolution and quality, often of definition 1024×1024 pixels or higher.

Local digital image correlation (DIC) based on cross-correlation was used to estimate the deformation of EBSD patterns since the advent of HR-EBSD [6], and was followed by other works [9, 10, 11, 4, 12], thanks to its speed and satisfactory uncertainty of the order of 10^{-2} pixel. The standard uncertainty of elastic strain measurement by local DIC has been estimated to be of the order of 10^{-4} [6]. Different ways to improve the measurement accuracy are discussed in Ref. [5], including increasing the exposure time, selecting full resolution (*i.e.*, no pixel binning) or using software integration instead of hardware integration, using high digitization depth to record gray levels, and placing the detector close to the sample. Different physical quantities have been assessed by HR-EBSD with high accuracy, ranging from elastic strain and stress [6], geometrically necessary dislocations [13], local misorientations [14] and slip activities [15]. These measurements via HR-EBSD also enrich numerical simulations. For example, the elastic strains measured by HR-EBSD have been successfully compared to crystal plasticity finite element simulation for single crystal [15] and polycrystals [16] samples.

Today, commercial softwares exist such as “BLG CrossCourt” [17]. Several laboratories have developed their own software for HR-EBSD analyses (*e.g.*, “StrainCorrelator” [18] or “Phase-Only-Correlation” (POC) [9]). They are all based on cross-correlation analyses. The challenges linked with data processing by cross-correlation are identified as follows:

1. Every ZOI provides a mean displacement. For a good accuracy of cross-correlations, the size of the ZOI should be large enough to contain a sufficient number of Kikuchi bands. In order to get a rich displacement field, it is mandatory to take a large number of ZOIs (in practice varying between 25 and 100 [18, 17, 8]). Due to the large number and size of ZOIs, a significant overlap is present in ZOIs (Figure 10). This step is slow and does not reduce the resulting uncertainty because of the very strong correlations that are present. Thus the invested computation time has a low return in terms of quality since the pixels of the diffraction image are calculated many times in different ZOIs.
2. The strain measurement in cases of relatively high misorientation angles ($\geq 1^\circ$) between reference and registered EBSD patterns. For displacement fields composed of pure translations of image subsets, the kinematic basis is no longer adapted to reproduce the observed image transformations. Consequently, cross-correlation may yield errors such as abnormally high stress levels at zones with high rotations compared with the reference image. Different approaches have been proposed to solve this problem, such as the “remapping” technique [10, 11], which rotates the reference EBSD pattern to make it resemble better the studied image.

However, the imprecise PC value limits the performance of remapping [15]. Another proposition consists in adopting numerous intermediary reference EBSD images inside the same grain [17]. This demands that when a studied EBSD pattern exhibits a misorientation angle with respect to the reference image greater than a chosen threshold, the targeted EBSD pattern is chosen as the new reference for nearby EBSD patterns. In the end, the misorientation field with respect to a unique reference image could be obtained by multiplying the measured deformation gradient tensor with respect to the intermediary reference image. However, the uncertainty is accumulated in this approach.

Very recently, Vermeij and Hoefnagels have proposed an Integrated DIC (IDIC) framework dedicated to HR-EBSD [19]. In this approach, the physical relationship between the distortion of EBSD patterns and the elastic strain for the studied crystal was considered as exact, and only the corresponding few degrees of freedom describing the elastic strains are considered for registering EBSD patterns. It was shown that IDIC allows low levels of uncertainty to be achieved for the deformation gradient measurement, while showing tolerance to large rotations and large strains between the reference and current EBSD patterns. However, these results were obtained via virtual experiments, for which a small set of *artificial* (*i.e.*, computed) EBSD patterns was analyzed. No comparison with DIC-remapping methods, which are currently used in several laboratories, were proposed. The remarkable robustness to noise is impressive. However, only an ideal white Gaussian noise was considered on the diffraction images, and different physical phenomena encountered experimentally, such as background issues, contrast changes, pattern evolutions may be suspected to also play a significant part in the final uncertainty of the method. In addition, the implementation was reported as slower than conventional (and already slow) DIC and remapping techniques.

The present work also proposes an IDIC framework, very similar in spirit to that of Vermeij and Hoefnagels [19], although developed independently [20]. Section 2 details the IDIC data processing for HR-EBSD. Section 3 re-evaluates a 1D profile of a limited-strained monocrystal sample, for which quantitative comparisons with the results provided previously by an existing HR-EBSD software as well as those of Laue diffraction [15] are proposed. Section 4 studies 2D fields of deformation gradient tensors for a commercial grade austenitic stainless steel covering a wide range of stresses. Moreover, the specific implementation of the IDIC method proposed herein turns out to be much faster than previously proposed local-DIC and remapping techniques.

2 Integrated DIC for HR-EBSD: ADDICTED

An alternative to cross-correlation of ZOIs (also known as local DIC) has been proposed as global DIC [21, 22] or integrated DIC [23, 24, 25]. The global image registration approach to HR-EBSD through iterative remapping was first proposed by Maurice [26]. The differences between two EBSPs before and after registration were presented, showing an overall reduction. Yet all the advantages of the approach were not thoroughly explored. The global approach uses the entire ROI (and only once) instead of many ZOIs. The repetitive calculations of the same pixels and the empirical choice of ZOIs naturally disappear, together with the issue of dealing appropriately with correlations of measurement due to overlapping ZOIs [27]. Besides, global DIC provides a residual field, which is calculated at each pixel and constitutes by nature a good criterion to characterize the registration error. It should

be noted that the registration error has been characterized since the beginning of HR-EBSD technology by the cross-correlation quality, more explicitly the cross-correlation function (XCF) peak intensity averaged over the set of ZOIs. Yet more information is presented in the residual field of IDIC, as will be demonstrated in Section 2.2.4.

Integrated Digital Image Correlation (IDIC) has been proposed to measure *directly* the physical quantities (parameters) of interest from image registrations. Thus the measured displacement fields are expressed in a “kinematic basis” that is tailored *a priori* to the studied physical phenomena (and potentially the artifacts of image formation and acquisition). The projection geometry of EBSD patterns is briefly recalled in Appendix 5 together with the definition of several notions used in the paper. The HR-EBSD technique is mainly based on Equation (31), and all the following analyses discuss its exploitation. No additional degrees of freedom are allowed in the displacement field. This technique can be adapted to HR-EBSD analyses since it is based on an interpretative framework adjusted to the expected kinematics, and exploits the pixels of each image with an equal weight.

A new IDIC-based algorithm has been developed to measure elastic strains from HR-EBSD images [19]. A similar algorithm, together with the necessary pre-processing of diffraction images proposed herein, is summarized in Figure 1 and detailed in this section. It has been proposed to call the new method ADDICTED, an acronym for “Alternative Dedicated Digital Image Correlation Tailored to Electronic Diffraction.”

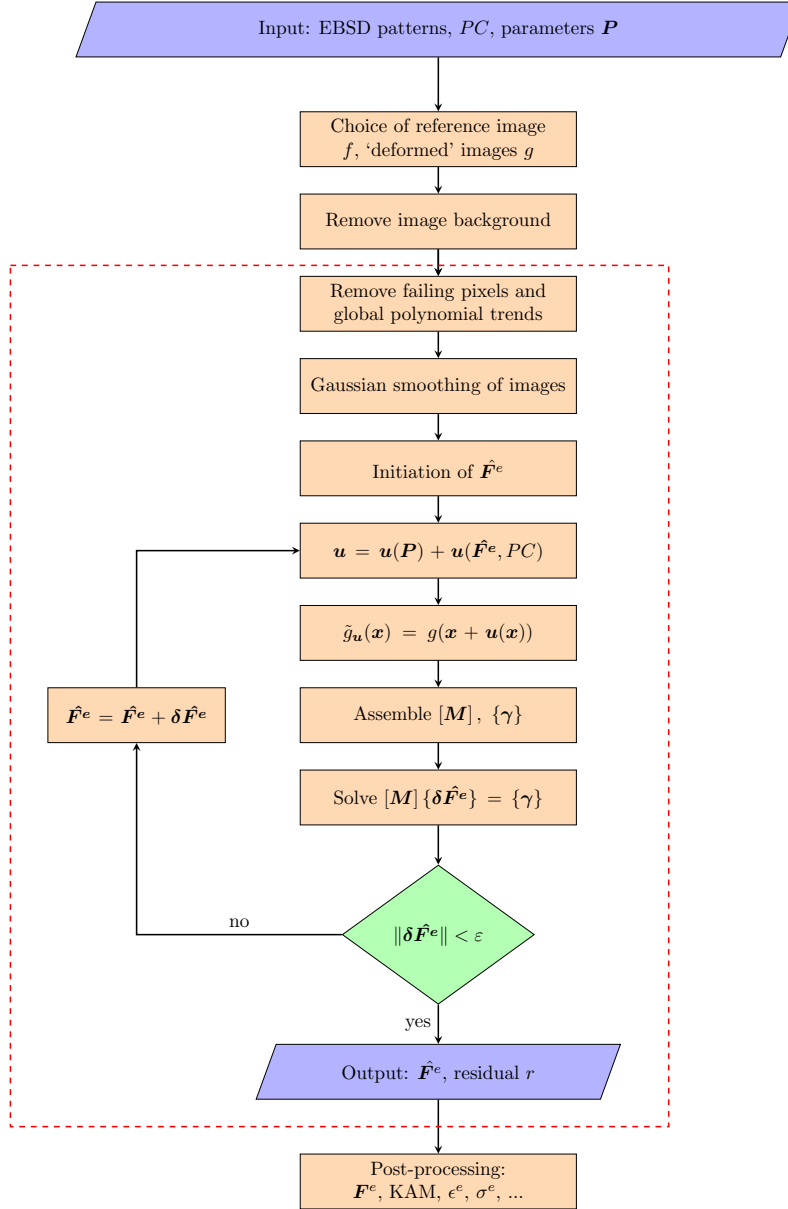


Figure 1: Flowchart of the ADDICTED algorithm. The steps included in the box are exclusive to ADDICTED. The input \mathbf{P} parameters sum up all those that influence the displacement fields other than the elastic deformation gradient tensor (*e.g.*, beam-induced shift and sample inclination, see Section 2.2.1).

2.1 Picture preparation

2.1.1 Subtraction of background

The acquired images include a gray level background mainly due to the uneven energy distribution of the diffracted electrons. For example, the raw diffraction image shown in Figure 2(a) indicates that the intensity is higher at the image center than its periphery. The EBSD shown here have a circular shape since a circular aperture was placed in front of the detector, blocking all electrons outside its opening [28]. It is common practice to correct the images by subtracting or dividing by the background [29, 30]. An EBSD acquisition is performed at low magnification

for a polycrystal to scan a big number of grains of different orientations. The corresponding diffraction images are averaged to estimate the gray level background of the EBSD setup. The diffraction images with subtracted background are referred to as “corrected images,” as shown in Figure 2(b). Kikuchi bands are clearer in Figure 2(b) than Figure 2(a). However another low-frequency gray level variation is visible. These corrected images are the starting point of all the following analyses.

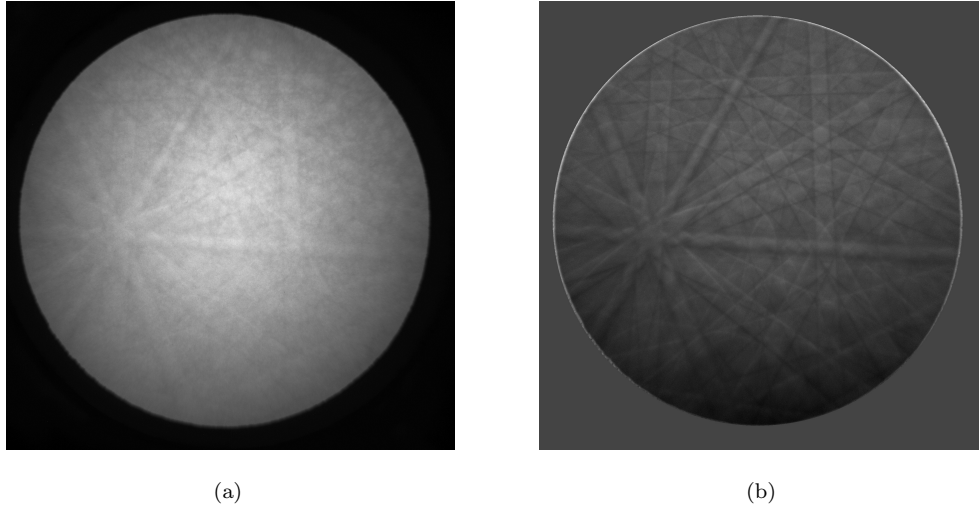


Figure 2: Example of background correction. (a) Raw diffraction image. (b) Corrected image (provided by CrossCourt [17]). The chosen image shows that the correction is not always completely satisfactory.

2.1.2 Filtering of bad pixels

Because of the non-uniformity of the phosphorescent screen utilized for electron capture, the acquired images often contain, at fixed locations, over-exposed or under-exposed pixels due to scratches. These very bright pixels are detrimental to DIC calculations and it is proposed to replace the gray level of these “bad pixels” by the mean values of neighboring pixels.

The key point is to locate the bad pixels. Some of them are easy to locate by calculating the difference before and after low-pass filtering. Some others are more difficult to find since their contrast with neighbors is not significantly higher than pure noise, yet, their intensity is systematically depressed or amplified with respect to their expected levels. In that case, a pre-calculation of 50-100 EBSPs and averaging their residual maps reveals each ‘bad pixel’ as a pair of high (in absolute value) residual points on the averaged residual map. Pin-holes and scratches on the phosphor will be revealed in the same way. It is found that eliminating the ‘bad pixels’ (*i.e.*, by replacing them by the average of their neighbors) not only decreases the uncertainty of HR-EBSD, but also significantly improves the convergence speed.

2.1.3 Extraction of global variation of gray levels

After the extraction of the diffraction image background, the Kikuchi bands may possess global variations in gray levels, which are related to the fluctuations of the average energy of diffracted electrons. For example, Figure 3(a) shows a diffraction image brighter in the upper part and darker in the lower part. This global tendency impacts less

the quality of cross-correlation, which studies “local” ZOIs of the image. However, for global image registration, it is preferable to subtract the global gray level changes, which are assumed to be represented by a polynomial of order 2 or even higher (obtained by a classic regression procedure). One may choose high-order polynomials if the global gray level trend is very irregular. Otherwise, it is suggested to keep the order as low as possible to avoid spurious peaks. A polynomial of order 2 was subtracted in the second experimental case in the paper, but not on the first one due to its high-quality EBSPs. After the extraction of the global gray level variations, the EBSPs have an average gray level of 0. Then the gray level of all pixels is re-scaled so that its standard variance is 1. Finally, all the gray levels are truncated between -3 and 3 to reduce the effect of existing over-bright and over-dark pixels. The beneficial effect of this second-order polynomial subtraction is shown in Figure 3, where Figure 3(a) is transformed into Figure 3(b), which is more uniform and the contrast related to Kikuchi bands is more visible.

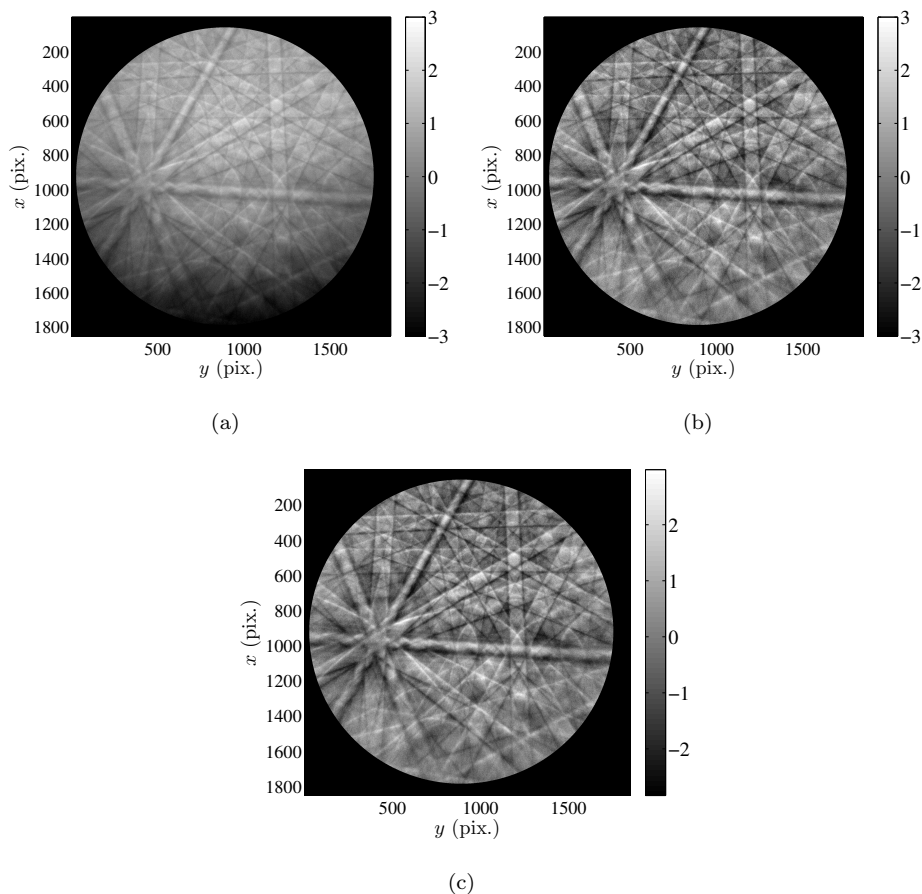


Figure 3: Effect of gray level correction and Gaussian filtering. (a) Diffraction Image truncated between -3 and 3 . The average gray level is 0 and the standard deviation is 1. (b) Previous image corrected by subtraction of a second-order polynomial fit. (c) Previous image filtered by Gaussian kernel of $\xi = 1$ pixel. The convolution with Gaussian filter eliminates efficiently the high frequency noise from diffraction images.

2.1.4 Filtering of high frequency noise

Gaussian filtering at very small scales of the EBSD pattern makes the subsequent calculations faster because the raw image was corrupted by very high frequency white noise. A comparison of convergence speed with and without

Gaussian filtering on an experimental case is provided in Section 4. The effect of Gaussian filtering \tilde{f} is illustrated in Figures 3(b) and 3(c). The smoothing involves the convolution of the initial image f by a Gaussian kernel G

$$\tilde{f} = f * G \quad (1)$$

where $G(x, y)$ is chosen as Gaussian depending on an internal length ξ

$$G(x, y) = \frac{1}{2\pi\xi^2} e^{-\frac{x^2+y^2}{2\xi^2}} \quad (2)$$

In practice, the chosen length ξ ranges between 1 and 2 pixels. This choice depends on the noise level of the image, which is in turn dependent on the acquisition time, the pixel number, the electron beam parameters and the imaged material.

2.2 Algorithm

2.2.1 Correction of projection parameter variations

The projection parameters such as the coordinates of the projection center (x^*, y^*, z^*) and the relative inclination angle between the sample and the screen are important in HR-EBSD analyses. The effects of scanning on EBSPs should be removed in the so-called ADDICTED technique, and it should be noted that the scanning correction and the final results of HR-EBSD are limited by the accuracy of the projection parameters [31].

- *Beam-induced shift*

When running ADDICTED calculations, the shift of the EBSD images due to motions of the emission point (in other words the scanning motion of the electron beam) should be corrected, as revealed by the initial HR-EBSD analyses [6]. This shift, \mathbf{w} , is obtained precisely by the SEM calibration with a standard specimen, knowing the scanning direction on the screen and the physical size of the screen pixel. This correction of a global translation of the image by \mathbf{w} reads

$$\hat{g}(\mathbf{x}) = g(\mathbf{x} + \mathbf{w}) \quad (3)$$

where \hat{g} is the corrected image, and can be performed via cross-correlation over the whole ROI. It is worth noting that \mathbf{w} only depends on the position of the incident electron beam, and for each diffraction image Equation (3) describes a pure translation.

- *Correction of relative inclination of the sample*

The sample is tilted to about 70° for HR-EBSD acquisitions and the screen is tilted by several degrees too. If the acquisition is carried out on a large zone (say greater than $100 \times 100 \mu\text{m}^2$), the distance between the emission point and the screen, z^* , varies in a non negligible manner. It is noteworthy that varying z^* induces magnification changes. Therefore, the size of the diffraction image should be adjusted, centered about the PC, $\mathbf{x}^* = (x^*, y^*)^\top$, before launching ADDICTED

$$\check{g}(\mathbf{x} - \mathbf{x}^*) \equiv \hat{g} \left[\left(\frac{z_g^*}{z_f^*} \right) (\mathbf{x} - \mathbf{x}^*) \right] \quad (4)$$

where z_g^* is the distance between the emission point and the screen for the deformed image, and z_f^* is that for the reference configuration. Consequently, the effects of the projection parameters on the displacement field are treated and corrected before and the final solution to the minimization problem is conducted for $\widehat{\mathbf{F}}^e$.

2.2.2 Global digital image correlation

Conventional DIC consists in correlating two gray level images, one of the reference state $f(\mathbf{x})$ and the other one of the deformed state $\check{g}(\mathbf{x})$. The displacement field $\mathbf{u}(\mathbf{x})$ between the two images is measured by correcting the deformed image $\tilde{g}_{\mathbf{u}}(\mathbf{x}) = \check{g}(\mathbf{x} + \mathbf{u}(\mathbf{x}))$ to match as best as possible the reference image $f(\mathbf{x})$, which involves the minimization of the quadratic norm of the residual $r = (f(\mathbf{x}) - \tilde{g}_{\mathbf{u}}(\mathbf{x}))$ summed over the entire ROI.

The cost function to minimize writes

$$\Theta = \sum_{ROI} (f(\mathbf{x}) - \tilde{g}_{\mathbf{u}}(\mathbf{x}))^2 \quad (5)$$

where $\tilde{g}_{\mathbf{u}}(\mathbf{x}) = g(\mathbf{x} + \mathbf{u}(\mathbf{x}))$ is the deformed image corrected by the measured displacement field (for the iterative algorithm, it is the current estimate). The minimization of the cost function leads to successive corrections of the displacement estimation until convergence [32]. The displacement field (or its corrections) is constructed by linear (or affine) combinations of fields constituting the kinematic basis. For ADDICTED, IDIC is the chosen tool to analyze diffraction images, namely, f and g are respectively the diffraction images of the reference crystal (*e.g.*, assumed to be stress-free), and of the deformed crystal. The displacement field \mathbf{u} observed in the diffraction images has to be related to the elastic deformation gradient of the diffracting crystal, $\widehat{\mathbf{F}}^e$.

$$\mathbf{u} = \mathbf{u}(\mathbf{x}; \widehat{\mathbf{F}}^e) \quad (6)$$

The displacement field usually has nonlinear dependencies with $\widehat{\mathbf{F}}^e$. First order Taylor expansions are performed

$$\mathbf{u}(\mathbf{x}; \widehat{\mathbf{F}}^e + \delta\widehat{\mathbf{F}}^e) = \mathbf{u}(\mathbf{x}; \widehat{\mathbf{F}}^e) + \Phi_i(\mathbf{x}; \widehat{\mathbf{F}}^e) \delta\widehat{F}_i^e \quad (7)$$

with

$$\Phi_i = \frac{\partial \mathbf{u}}{\partial \widehat{F}_i^e} \quad (8)$$

where Φ_i is the sensitivity field with respect to the component \widehat{F}_i^e ($i = 1, 8$) of the elastic deformation gradient tensor. As a result, for example, $[\Phi]$ is a matrix of size $(2N_{pixel}) \times 8$. To be explicit, by combining Equations (30)

and (31), the sensitivity fields read

$$\begin{aligned}
\Phi_{x1} &= \frac{z^*(x-x^*)}{\hat{F}_7^e(x-x^*) + \hat{F}_8^e(y-y^*) + z^*} & \Phi_{y1} &= 0 \\
\Phi_{x2} &= \frac{z^*(y-y^*)}{\hat{F}_7^e(x-x^*) + \hat{F}_8^e(y-y^*) + z^*} & \Phi_{y2} &= 0 \\
\Phi_{x3} &= \frac{(z^*)^2}{\hat{F}_7^e(x-x^*) + \hat{F}_8^e(y-y^*) + z^*} & \Phi_{y3} &= 0 \\
\Phi_{x4} &= 0 & \Phi_{y4} &= \frac{z^*(x-x^*)}{\hat{F}_7^e(x-x^*) + \hat{F}_8^e(y-y^*) + z^*} \\
\Phi_{x5} &= 0 & \Phi_{y5} &= \frac{z^*(y-y^*)}{\hat{F}_7^e(x-x^*) + \hat{F}_8^e(y-y^*) + z^*} \\
\Phi_{x6} &= 0 & \Phi_{y6} &= \frac{(z^*)^2}{\hat{F}_7^e(x-x^*) + \hat{F}_8^e(y-y^*) + z^*} \\
\Phi_{x7} &= -\frac{z^*(x-x^*) \left(\hat{F}_1^e(x-x^*) + \hat{F}_2^e(y-y^*) + \hat{F}_3^e z^* \right)}{\left(\hat{F}_7^e(x-x^*) + \hat{F}_8^e(y-y^*) + z^* \right)^2} & \Phi_{y7} &= -\frac{z^*(x-x^*) \left(\hat{F}_4^e(x-x^*) + \hat{F}_5^e(y-y^*) + \hat{F}_6^e z^* \right)}{\left(\hat{F}_7^e(x-x^*) + \hat{F}_8^e(y-y^*) + z^* \right)^2} \\
\Phi_{x8} &= -\frac{z^*(y-y^*) \left(\hat{F}_1^e(x-x^*) + \hat{F}_2^e(y-y^*) + \hat{F}_3^e z^* \right)}{\left(\hat{F}_7^e(x-x^*) + \hat{F}_8^e(y-y^*) + z^* \right)^2} & \Phi_{y8} &= -\frac{z^*(y-y^*) \left(\hat{F}_4^e(x-x^*) + \hat{F}_5^e(y-y^*) + \hat{F}_6^e z^* \right)}{\left(\hat{F}_7^e(x-x^*) + \hat{F}_8^e(y-y^*) + z^* \right)^2}
\end{aligned} \tag{9}$$

2.2.3 Solution

The minimization algorithm follows the standard IDIC steps without particular modification [32]. The cost function (5) is iteratively minimized with a Gauss-Newton algorithm. The column vector $\{\delta \widehat{\mathbf{F}}^e\}$ gathering all corrections to $\widehat{\mathbf{F}}^e$ is obtained

$$[\mathbf{M}] \{\delta \widehat{\mathbf{F}}^e\} = \{\gamma\} \tag{10}$$

where $[\mathbf{M}]$ is the Hessian matrix of size 8×8 at iteration $n-1$

$$M_{ij}^{(n-1)} = \sum_{ROI} (\nabla f(\mathbf{x}) \cdot \Phi_i(\mathbf{x}, \widehat{\mathbf{F}}^e)) (\nabla f(\mathbf{x}) \cdot \Phi_j(\mathbf{x}, \widehat{\mathbf{F}}^e)) \tag{11}$$

and the second member $\{\gamma_i\}$ includes the residual field

$$\gamma_i^{(n)} = \sum_{ROI} \left(f(\mathbf{x}) - \tilde{g}^{(n)}(\mathbf{x}, \widehat{\mathbf{F}}^e) \right) \nabla f(\mathbf{x}) \cdot \Phi_i(\mathbf{x}, \widehat{\mathbf{F}}^e) \tag{12}$$

When $\|\{\delta \widehat{\mathbf{F}}^e\}\| < \epsilon$, ϵ being chosen equal to 10^{-7} for all the calculations of this paper, the minimization stops and $\widehat{\mathbf{F}}^e$ is stored. Otherwise, $\widehat{\mathbf{F}}^e$ is updated

$$\widehat{\mathbf{F}}^e{}^{(n)} = \widehat{\mathbf{F}}^e{}^{(n-1)} + \delta \widehat{\mathbf{F}}^e{}^{(n)} \tag{13}$$

Once $\widehat{\mathbf{F}}^e$ is obtained, the displacement field \mathbf{u} is derived from Equation (30), and the deformed image can be corrected with these new estimates.

2.2.4 Analysis of noise

Besides $\widehat{\mathbf{F}}^e$, ADDICTED gives another important result, namely, the correlation residuals evaluated at any pixel location in the ROI

$$r(\mathbf{x}) = f(\mathbf{x}) - \tilde{g}(\mathbf{x}) \tag{14}$$

The registration residual r collects all artifacts of the formation and acquisition of EBSD patterns, and thus potentially contains very rich indications of the analyzed images. Signals in the residual that are not (white) noise often indicate an incomplete exploitation of the information, or an unadapted kinematic transformation between images. The residual may thus contain signal and noise. Let us assume that the reference image f is formed from a noiseless signal, f_p , with the superposition of a supposedly normal distributed noise b_f , which is known by the designation “Gaussian white noise”

$$f(\mathbf{x}) = f_p(\mathbf{x}) + b_f(\mathbf{x}) \quad (15)$$

The superposition is assumed to contain no spatial correlation. The same formation for a series of deformed diffraction images g^i reads

$$g^i(\mathbf{x}) = g_p^i(\mathbf{x}) + b_g^i(\mathbf{x}) \quad (16)$$

where b_g is white noise. After the application of ADDICTED, the corrected image reads

$$\tilde{g}^i(\mathbf{x}) = \tilde{g}_p^i(\mathbf{x}) + \tilde{b}_g^i(\mathbf{x}) \quad (17)$$

thus the residual reads

$$\begin{aligned} r^i(\mathbf{x}) &= f(\mathbf{x}) - \tilde{g}^i(\mathbf{x}) \\ &= f_p(\mathbf{x}) - \tilde{g}_p^i(\mathbf{x}) + b_f(\mathbf{x}) - \tilde{b}_g^i(\mathbf{x}) \\ &= b_f(\mathbf{x}) - \tilde{b}_g^i(\mathbf{x}) \end{aligned} \quad (18)$$

It is proposed to use $1 - \|r^i\|^2/\|f\|^2$ as a quality indicator of ADDICTED for the i th EBSP, and an example is shown in Section 4. Equation (18) can be established if the ideal reference f_p and deformed \tilde{g}_p^i images perfectly match after the registration.

The same reference image is utilized for a given grain, which means a unique image f is registered to a series of deformed images g . The residuals at convergence for all images g can be averaged and, by noting $\langle \dots \rangle$ their average over the different points inside one grain,

$$\begin{aligned} \langle r^i \rangle &= b_f - \langle \tilde{b}_g^i \rangle \\ &= b_f \end{aligned} \quad (19)$$

The average of the residual field provides an estimation of b_f , which allows noise to be removed from the reference image, f_p . The “cleaned” reference image allows the measurement uncertainty to be decreased (*i.e.*, variance divided by 2).

The ADDICTED algorithm has been implemented in Matlab. The code enables all the reported results labelled ADDICTED or integrated image correlation to be obtained. The proposed algorithm has been tested on two sets of experimental data. The first test was performed by Plancher [8, 15] and analyzed with StrainCorrelator. The published data from this study were used to quantify the uncertainty of ADDICTED with respect to one HR-EBSD software, on this very careful experiment of a “pure” case based a monocrystal sample. The second test probes the feasibility of the algorithm in a more realistic case (*i.e.*, a more complex polycrystalline material). In the latter case, the performance of ADDICTED is compared with the results obtained with the CrossCourt software.

3 Single crystal sample in 4-point flexural test

A 4-point flexural test on a single crystal sample, which was performed by Plancher [8, 15], was designed to cross-validate elastic strain measurements by HR-EBSD and DIC-Laue techniques. A brief description of the flexural test is given in Appendix B. The interested reader is referred to the two aboved cited publications for a more detailed description of the test. All the results marked as DIC-Laue and StrainCorrelator are extracted from Ref. [15] (courtesy of Dr. Plancher). It should be noted that remapping was not performed by StrainCorrelator on this bending test, as rotations (and strains) are small. The very same EBSPs of this study were processed with ADDICTED for comparison purposes.

According to beam theory, a neutral axis where there is neither compression nor tension exists at the sample mid-height along the longitudinal direction. Therefore, the test provides a reference diffraction image, which corresponds to an unloaded state, at the intersection of the studied profile and the neutral axis, denoted by point **O** in Figure 18.

Two different ROIs are used in ADDICTED. The first one, shown in Figure 4(a), includes the pixels inside the ZOIs of StrainCorrelator [8]. The second one (see Figure 4(b)) considers almost the entirety of the reference EBSP.

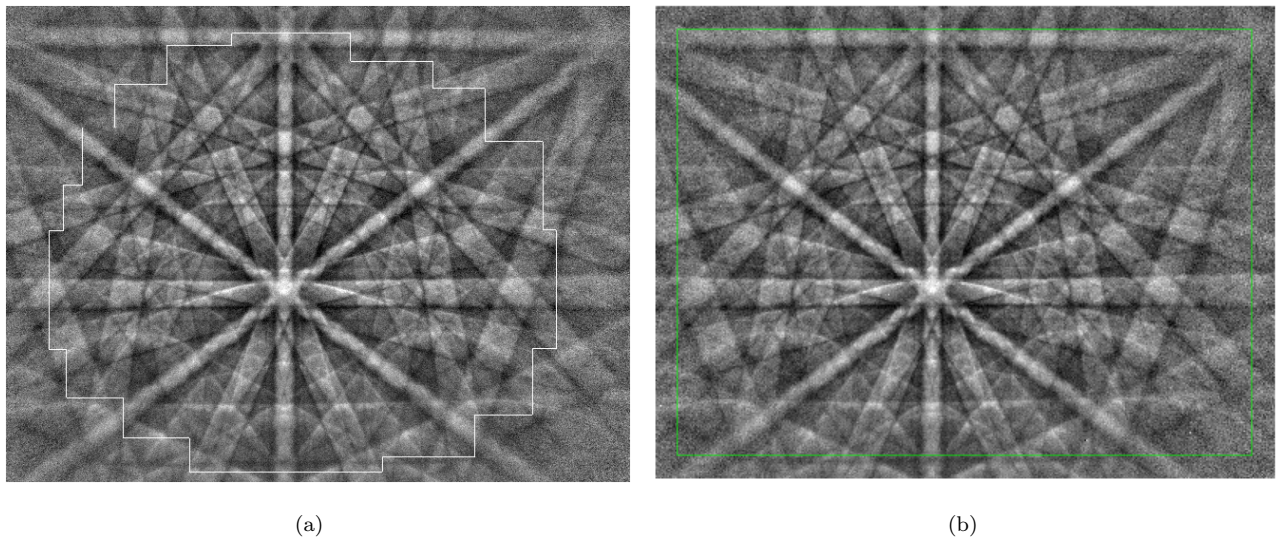


Figure 4: Two ROIs used by ADDICTED. (a) Originates from the 24 ZOIs used by StrainCorrelator [8]. The serrated edges indicate the outer boundaries of all the ZOIs. (b) Considers almost the entire EBSP, and is referred as ‘big rectangular ROI’ hereafter.

The strain component ϵ_{yy} corresponds to the direction along which the strain level is the highest. Its profile, treated by both StrainCorrelator and ADDICTED, is shown in Figure 5. It is worth noting that in order to make the HR-EBSD and Laue-DIC results more consistent, the reference point of Laue-DIC was shifted rightward by $12\ \mu\text{m}$ as compared to Refs. [8, 15], and \mathbf{F} was adjusted accordingly, which approximately shifts the Laue-DIC ϵ_{yy} profile leftward by $12\ \mu\text{m}$ and upward by 1.2×10^{-4} . This change is based on the assumption that the reference points in HR-EBSD and Laue-DIC analyses are not the same, which is stated in Ref. [8]. The ϵ_{yy} profile calculated by StrainCorrelator is shown in Figure 5(a). The calculation by ADDICTED with the same parameters (Gaussian filtering with 1-pixel kernel, the same ROI and the same raw reference EBSP) as StrainCorrelator is shown in

Figure 5(b). As a result the scatter in data between Figures 5(a) and 5(b) provide a fair comparison of the performance of the two HR-EBSD algorithms.

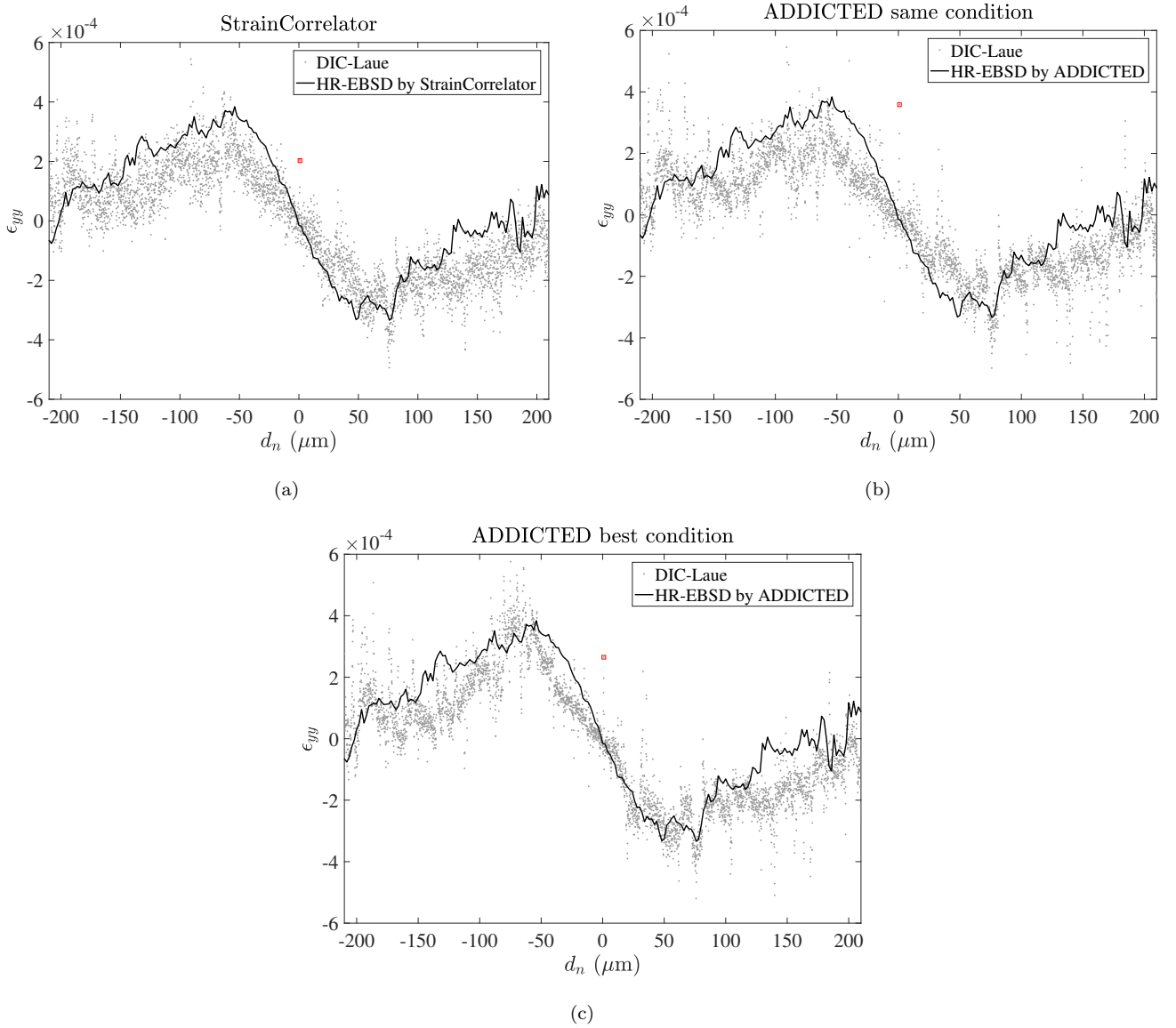


Figure 5: ϵ_{yy} profiles as functions of the distance to the neutral axis d_n , provided by (a) StrainCorrelator, (b) ADDICTED with the same raw reference EBSP, same ROI and same Gaussian filtering as StrainCorrelator. (c) ADDICTED with the ‘best computation conditions’ (bigger rectangular ROI, weighting against the noise level, no Gaussian filtering and using ‘cleaned’ reference EBSP as shown in Figure 8(c)). For comparison purposes, ϵ_{yy} profiles calculated by DIC-Laue [15] are drawn in all sub-figures.

Different computation conditions were tested for ADDICTED, such as the ROI size, Gaussian filtering kernel, raw or ‘cleaned’ reference EBSP. The best computation condition is using a large ROI of a ‘cleaned’ reference EBSP to treat raw target EBSP images (with no filtering) and weighting against the noise level as shown in Figure 6(d). The ϵ_{yy} profile of the ‘best computation conditions’ is shown in Figure 5(c). 5,000 acquisition points are reported as a function of the distance to the beam neutral axis. Between $-50 \mu\text{m}$ and $50 \mu\text{m}$, a linear trend is observed,

corresponding to the elastic deformation regime. The vertical width of the cloud of points indicates the scatter of data.

Since the sample stems from a single crystal, the scatter of the resulting strains along the profile allows the performance of HR-EBSD algorithms to be compared. To calculate the latter, an average strain profile has been evaluated by moving average of 100 consecutive data points, then the standard deviation of distances between the data points and the average profile was considered as the scatter. The standard deviation of ϵ_{yy} profiles, ς , for different sets of data is reported in Table 1. For the same computation parameters, ADDICTED resulted in consistently lower standard deviations than StrainCorrelator. By taking the same computation condition, the standard deviation is 5.6×10^{-5} for StrainCorrelator, and 5.5×10^{-5} for ADDICTED. If the stray points at activated slip locations are excluded in calculation, the value is 4.3×10^{-5} for StrainCorrelator and 3.6×10^{-5} for ADDICTED. When considering only the data points in the linear part, the standard deviation is 4.0×10^{-5} for StrainCorrelator and 3.4×10^{-5} for ADDICTED.

Table 1: Standard deviation ς for different parts of the ϵ_{yy} profiles shown in Figure 5

Treating software	StrainCorrelator		ADDICTED same condition		ADDICTED best condition	
Profile range	Total	Elastic	Total	Elastic	Total	Elastic
ς (for all the points) (10^{-5})	5.6	4.9	5.5	4.7	4.9	4.0
ς (with stray points excluded) (10^{-5})	4.3	4.0	3.6	3.4	3.4	2.8

By adopting the optimal conditions, *i.e.*, excluding stray points at activated slip locations, and using a ‘cleaned’ reference EBSP, ς equals 2.8×10^{-5} for ADDICTED, which is higher but of the same order of magnitude as the uncertainty level predicted by simulated EBSPs [19]. However, ADDICTED leads to strain results of consistently lower variance than a cross-correlation based approach. This uncertainty gain is explained because ADDICTED considers a large and unique ROI, *i.e.*, only one sampling on a large number of data. The sampling bias, which affects the cross-correlation by image ZOIs, has been avoided. This phenomenon shows the robustness of ADDICTED against image noise. Besides, the HR-EBSD results provided by ADDICTED are in better agreement with the DIC-Laue results, especially the slope of the linear part. Furthermore, it is worth noting that this test leads to very small strains (*i.e.*, less than 10^{-3}), and the rotation of diffraction images is limited. Therefore it is a favorable case to apply cross-correlation of ZOIs (for StrainCorrelator). In cases with larger strains, ADDICTED is expected to be even more advantageous.

The ϵ_{yy} profile of Figure 5 is characterized by local discontinuities and outliers. Although found in the same locations, the discontinuities are more significant in the ADDICTED results, thanks to its lower uncertainty, especially for the plastically-deformed zones. It was found that discontinuities of \mathbf{F}^e components correspond to the presence of activated slip traces [8]. At each discontinuity, several outliers exist. The residual fields associated with outliers, *i.e.*, at the activated slip traces, are shown in Figure 6. Apart from these outliers, the residual contains

only white noise (Figure 6(a)). For the outliers, an unaccounted-for signal remains in the residual, which is visible on the lower left part of Figure 6(b), and on the lower right part of Figure 6(c). This phenomenon shows that the diffraction images acquired in the direct vicinity of slip traces are more complex than regular diffraction images. A possible explanation is that plastic slip could cause crystal rotations, and on the two sides of a slip trace two lattices of slightly different orientations may interact simultaneously with the electron beam. This phenomenon is called “pattern overlap,” and its detrimental impact on elastic strain measurement accuracy has been studied [33]. This observation proves on the one hand the high sensitivity of ADDICTED to such cases. On the other hand this example shows that the residual image calculated for each correlation between diffraction images contains a very rich information, which reveals the failure of the transformation model in this particular situation. Signals in the residual field point at a way for potential interpretation in the future.

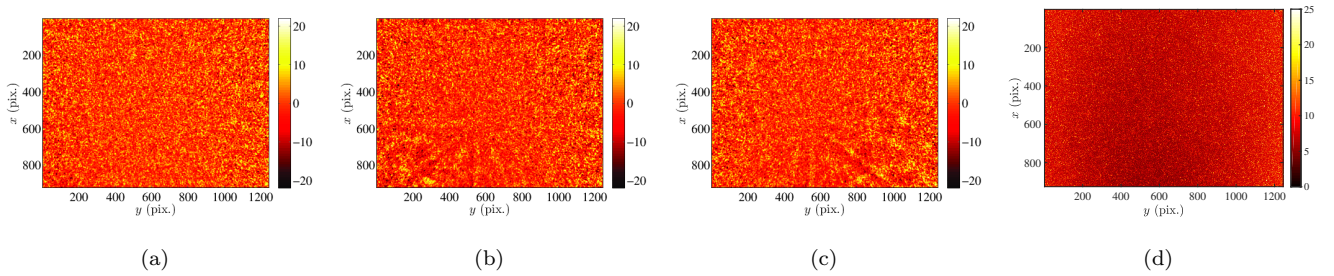


Figure 6: Residual field calculated by ADDICTED. (a): images outside the zone of localized slip trace. (b) and (c): residuals of diffraction images captured on the slip trace. (d): RMS of 90 residual fields, it’s visible that higher noises exist at the peripheral regions.

A few outliers exist in the linear part of the HR-EBSD results where no plasticity and thus pattern overlap is supposed to be present. It has been found that the EBSD patterns of the outliers tend to be partly degraded. The corresponding image registration residual cannot be reduced to pure white noise. An example of the residual field corresponding to the outlier in the linear part is given in Figure 7, where the EBSD patterns remain in a significant part of the image. Ideally, the formation mechanism of degraded EBSPs needs to be explained and induce the signals in the residual field to disappear, which is beyond the scope of the current paper.

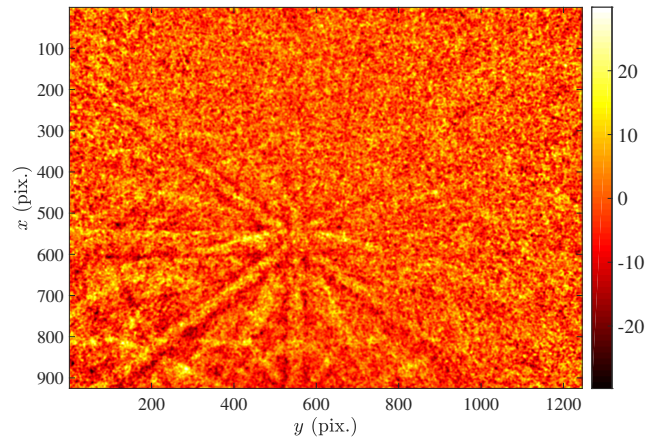


Figure 7: Residual field corresponding to the outlying point highlighted in Figure 5.

Figure 8 shows an example of denoising with the method explained in Section 2.2.4. The raw diffraction image is shown in Figure 8(a), where noise is clearly visible. In Figure 8(b), the diffraction image is reported once filtered with a Gaussian kernel of 2 pixels, thereby leading to an attenuation of noise but also a loss in image contrast. Figure 8(c) shows the denoised reference image based on ADDICTED results on 400 diffraction images located between $-40\ \mu\text{m}$ and $0\ \mu\text{m}$. Figure 8(c) reports a drastic reduction in noise while keeping the contrast of the original image. These trends are more manifest on the zoomed areas (Figures 8(d), 8(e), and 8(f)). Figure 8(f) reveals very rich details that are otherwise invisible in Figures 8(d) and 8(e).

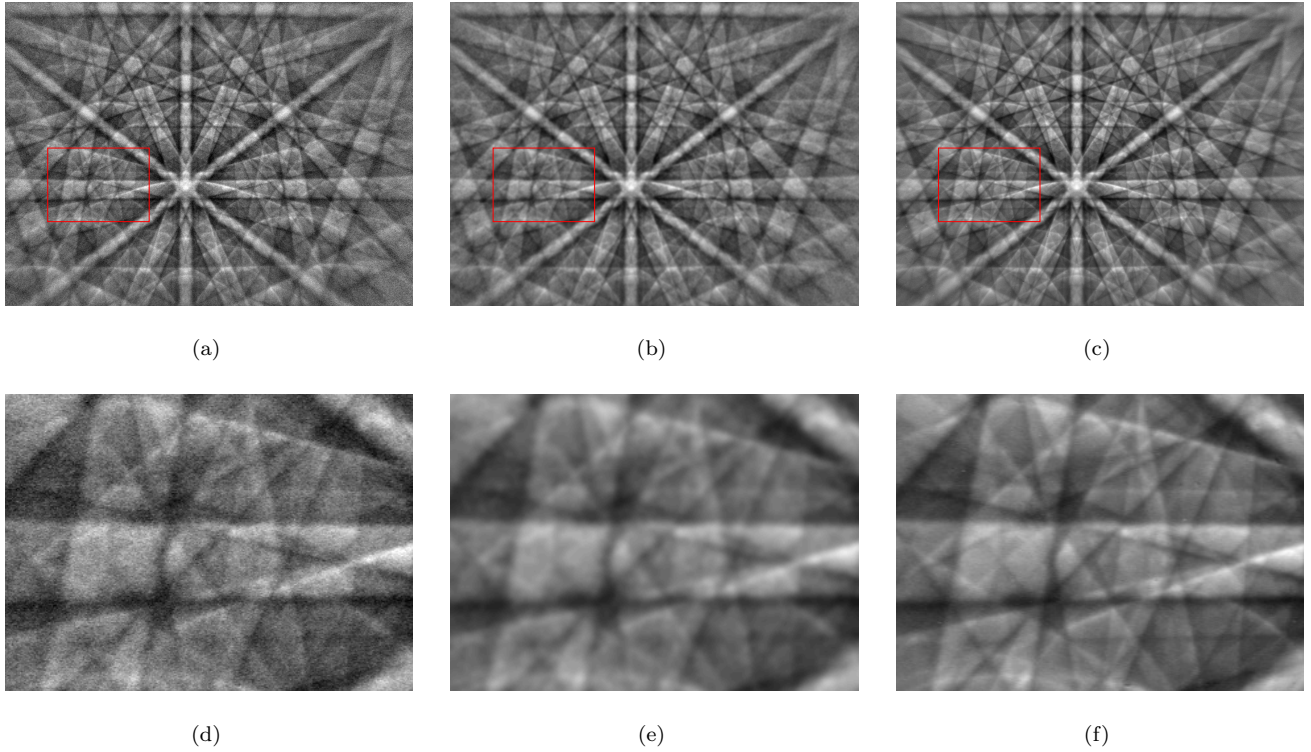


Figure 8: Example of noise reduction on a diffraction image. (a) Raw image. (b) Image filtered by convolution with a Gaussian kernel of length 2 pixels. (c) Denoised image with the method explained in Section 2.2.4. (d-f) Zooms of zones indicated by the red boxes in (a-c). It is seen that (c) and (f) show a significant decrease of noise while preserving the contrast of the Kikuchi bands.

For the flexural test on a single crystal sample, the present algorithm gives results with an uncertainty slightly lower than StrainCorrelator by adopting the same computing parameters. An optimal computing condition is identified thanks to this test, which further reduces the uncertainty level. The registration residual *field* shows a high sensitivity to localized phenomena.

4 Tensile test on polycrystalline sample

A more complex experiment has been performed to test the robustness of ADDICTED on an industrial material. An A316 stainless steel sample, having large grains, has been polished and subjected to an *in-situ* tensile loading

inside the chamber of a Tescan Mirra SEM (Figure 9). Pt speckles were deposited onto the sample surface in order to make kinematic measurements easier, which are not detailed herein. The Pt speckles appear as tiny bright dots in Figure 9(a) and do not significantly deteriorate the EBSPs of HR-EBSD. The three elliptical dark spots correspond to a Kossel X-ray diffraction study (not detailed hereafter), and three other spots are pitting corrosion spots created during electrochemical polishing, which prevent adequate EBSPs from being acquired. As a result, three dark spots are visible in Figure 9(b). The un-indexed pixels that are linearly arranged are also due to electrochemical polishing. It is believed that an emerging dislocation has provoked this accelerated etching. An in-situ rig (Micromeca) was used for performing the tensile test. The loading direction is horizontal in Figure 9 and the loading rate was 10^{-2} min^{-1} . At first plastic straining, HR-EBSD acquisitions have been performed on a ROI focused on a triple point of the microstructure. The working distance for HR-EBSD acquisitions was 16.3 mm, electron acceleration voltage was 30 kV, the probe current was 20 nA, and the exposure (dwell) time was 0.35 s. EBSD patterns were recorded at full definition (*i.e.*, 2048×2048 pixels), and each pattern was the result of averaging three frames. A square area of $100 \mu\text{m} \times 100 \mu\text{m}$ was indexed, and the step size was 70 nm in both directions.

ADDICTED has been used again to process these data. For comparison purposes, CrossCourt was also run including the remapping procedure on the same data set. The parameters are chosen to be identical for the two calculations (*i.e.*, coordinates of projection centers). Please note that after a first analysis, the reference point of the upper grain for ADDICTED was moved to a region with lower rotation gradient. This is unfortunately not possible for CrossCourt as the raw data was discarded due to its sheer size. Yet the two lower grains are calculated with the same reference points.

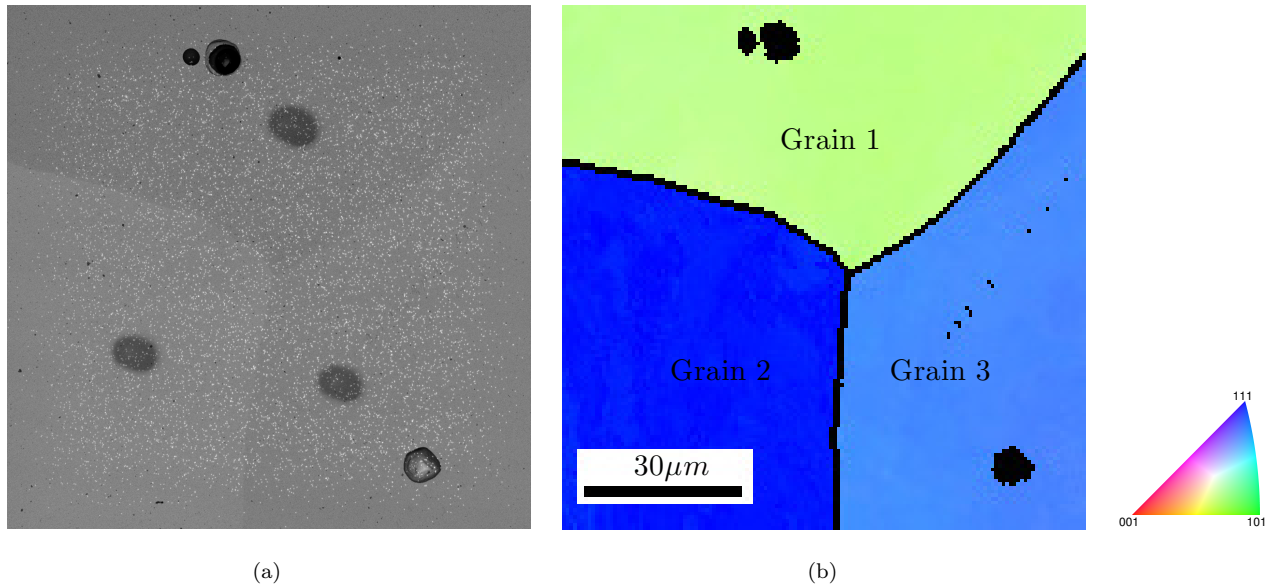


Figure 9: Region of interest of the sample. (a) Secondary electron image. (b) Crystallographic orientation of the ROI, as measured by standard EBSD analyses, which is observed to be virtually uniform within each grain.

Figure 11 shows an example of integrated correlation result on two diffraction images (a-b). A circular ROI, which is highlighted in blue in Figure 11(a), was adopted in the computation, and a margin is left outside the ROI to prevent the sought Kikuchi bands from falling outside the deformed EBSD pattern. Such margin should be broader

in cases of severe rotation/deformation of the studied grain. A rotation, which was not easily detected by bare eyes, exists between Figures 11(a) and 11(b). Yet it becomes notable when the difference between the two diffraction images is computed (Figure 11(c)). The 8 components of $\widehat{\mathbf{F}}^e$ are obtained by ADDICTED and the corresponding displacement fields are shown in Figures 11(e) and 11(f). Compared to DIC based on cross-correlation, the advantage of integrated correlation is noteworthy, namely, the displacement field is much richer. The rotation is intrinsically recovered by the algorithm, and does not need any “remapping” step, which is computationally costly.

Figure 11(g) shows the deformed image corrected by the measured displacement field, and Figure 11(h) the residual map between Figures 11(a) and 11(g). It is concluded that the dominant initial difference (Figure 11(c)) disappears and “phantom” bands become visible in the residual. Compared to the residuals obtained in the first example (Figure 6), the present residual map contains more information (Figure 11(h)) because the sample microstructure is more complex than the single crystal studied previously. Thus the diffraction images are less sharp. For instance, single slip traces create signals in the residual field (Figures 6(b) and 6(c)). A complex industrial polycrystalline sample with more slip traces and lattice distortions will inevitably lead to more unaccounted for motions. Further, as opposed to the previous case, it is not easy to select a stress-free point as reference and there might well be no strictly stress-free point at all. Let us stress that this difficulty is common to all HR-EBSD techniques and is not related to the specific algorithm used to evaluate crystal strains.

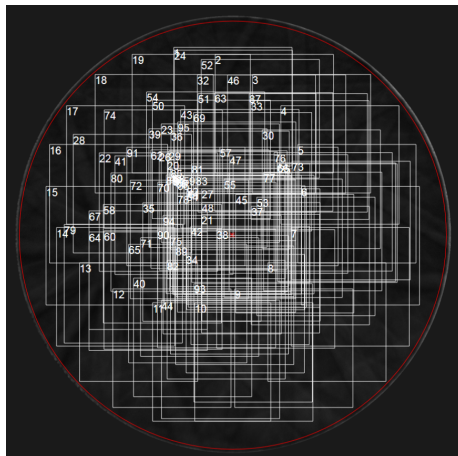


Figure 10: Example of distribution of 96 ZOIs used by CrossCourt [17] for performing cross-correlation calculations. A significant overlap is observed especially at the image center.

By observing the diffraction image in Figure 11(i), similarities between the Kikuchi bands and the “phantom” pattern in the residual are revealed (Figure 11(h)). This phenomenon indicates that the “background” of diffraction images has not been acquired satisfactorily. Consequently, the diffraction signal of grain 3 is contained in the corrected diffraction images of grain 1. By analyzing the residual field provided by ADDICTED, it is possible to reveal some information that would be hidden otherwise, which is useful to construct a better “background” image.

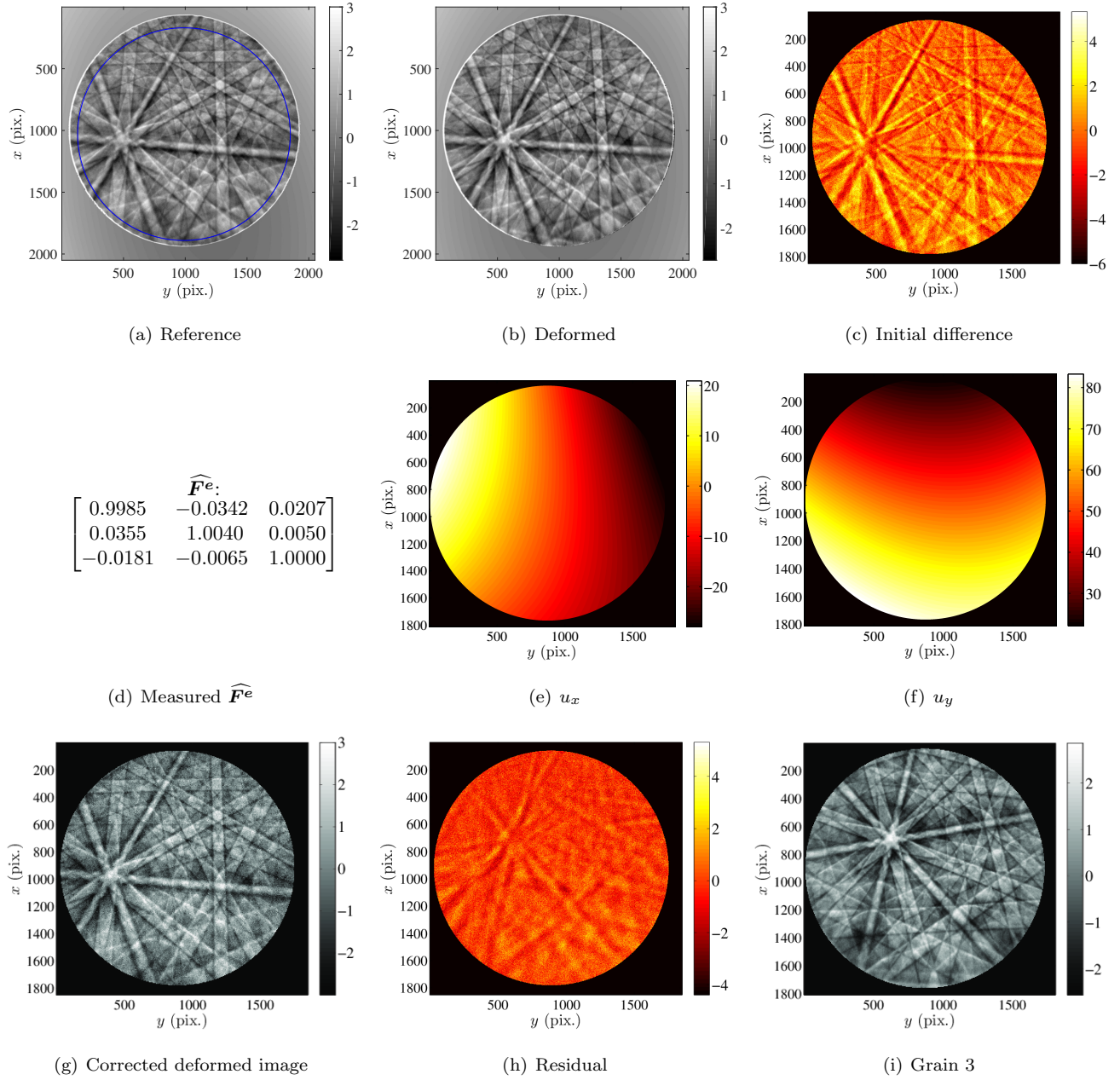


Figure 11: Example of integrated correlation result. (a) Reference and (b) deformed images of grain 1. The circular ROI is highlighted in blue in sub-figure (a) (c) Initial difference between the two images. (d) Tensor \mathbf{F}^e obtained by integrated correlation. Displacement field component along x (e) and y (f) directions (expressed in pixels). (g) Deformed image (b) corrected by the measured displacement field. (h) Corresponding residual (*i.e.*, difference between images (a) and (g)). (i) Diffraction image of grain 3, where a pronounced correlation with (h) is visible.

When using ADDICTED, it is preferable to start the calculation with images near the reference point. To initialize the first integrated calculation (*i.e.*, the first “deformed” diffraction image), the identity matrix \mathbf{I} is a good choice for $\widehat{\mathbf{F}}^e$, due to the assumed small strains between those images. To initialize the calculations over other pixels, it is generally recommended to take the value of $\widehat{\mathbf{F}}^e$ calculated for its immediate neighbors since the strains

are assumed to be close for nearby material points.

The convergence speed as a function of the computation conditions is summarized in Table 2. It is concluded that Gaussian filtering of diffraction images drastically reduces the number of iterations before convergence. The smoothing with a larger kernel (*i.e.*, 2 pixels) is more efficient than a smaller one (1 pixel). The initialization with $\widehat{\mathbf{F}}^e$ of neighboring pixels also accelerates convergence, especially for the computations on unfiltered diffraction images. The cleaned reference EBSP for each grain is obtained by averaging 100 residual maps.

Table 2: Number of iterations before convergence as a function of computation parameters

Computing conditions	raw, 2-pixel filter	raw, 1-pixel filter	raw, no filter	clean, no filter
Initialized by \mathbf{I}	17	65	700	50
Initialized by neighboring $\widehat{\mathbf{F}}^e$	14	50	300	15

The plane stress hypothesis has been used and $\widehat{\mathbf{F}}^e$ is transformed into \mathbf{F}^e . The emission zone (*i.e.*, interacting with the electron beam) is less than 25 nm deep [8], which legitimizes this hypothesis. It should be noted that the surface normal is assumed well known. Recently it has been shown that the topography can be evaluated accurately by DIC analyses on conventional SEM images taken at EBSD (also HR-EBSD) positions [34]. HR-EBSD acquisitions have been performed at the onset of plasticity thus it is legitimate to neglect the changes of topography. It is assumed that the rotation levels could be significant, yet the deformation contributions remain limited (elastic regime). Therefore, it is advised to keep the finite strain formalism for \mathbf{F}^e , and calculate the rotation \mathbf{R}^e tensor by polar decomposition

$$\mathbf{F}^e = \mathbf{V}^e \mathbf{R}^e \quad (20)$$

It has been found that the left side decomposition of \mathbf{F}^e is more convenient to implement for HR-EBSD, since when measuring the strains of the “deformed” region, one is interested in the strain of the crystal in the “deformed” configuration, that is the finite rotation between the reference and the current pattern is applied first, followed by an elastic distortion of the rotated crystal [10]. Then, the elastic right Cauchy Green and Green-Lagrange tensors are computed. If the strains remain small, the left Cauchy-Green tensor reduces to

$$(\mathbf{V}^e)^\top \mathbf{V}^e \simeq \mathbf{I} + 2\boldsymbol{\epsilon} \quad (21)$$

where $\boldsymbol{\epsilon}$ denotes the infinitesimal strain tensor [10].

The Kernel Average Misorientation (KAM), or local misorientation, is a property that characterizes the local deformation level of a crystal [7]. In the present case, the KAM is defined as

$$\text{KAM}_{ij} = \langle \varphi (\mathbf{R}_{ij} (\mathbf{R}_{neigh})^{-1}) \rangle \quad (22)$$

where \mathbf{R}_{ij} is the rotation tensor calculated at pixel (i, j) , \mathbf{R}_{neigh} the average of the rotation tensors at the 4 neighboring pixels, *i.e.*, $\mathbf{R}_{(i-1)j}$, $\mathbf{R}_{(i+1)j}$, $\mathbf{R}_{i(j-1)}$, $\mathbf{R}_{i(j+1)}$, and

$$\varphi(\mathbf{Q}) = \text{Arccos} \left(\frac{\text{tr}(\mathbf{Q}) - 1}{2} \right) \quad (23)$$

is the function that links a rotation tensor \mathbf{Q} to the misorientation angle. As illustrated in Figure 12(a), the KAM provided by standard EBSD analyses is too noisy to characterize a misorientation of the order of $10^{-4} - 10^{-3}$ rad. The indexing of crystallographic orientations by standard EBSD comes with an error of 0.5° . ADDICTED gives results (Figure 12(b)) very close to those obtained by CrossCourt (Figure 12(c)), which shows that the two HR-EBSD algorithms are equally successful in measuring the rotation gradients. It is worth noting that the reference EBSP for each grain should be chosen at a region with small KAM. Otherwise, the evaluated stress level for the grain could exhibit an overall stress that is opposite to the stress state of the reference point. The inter-granular straight traces are due to polishing artifacts/scratches and appear in the two images, as highlighted by ellipses in Figures 12(b) and 12(c). Further, the KAM is higher at grain boundaries, especially at triple points, which is consistent with dislocation pile-up [35] and experimental observations [36].

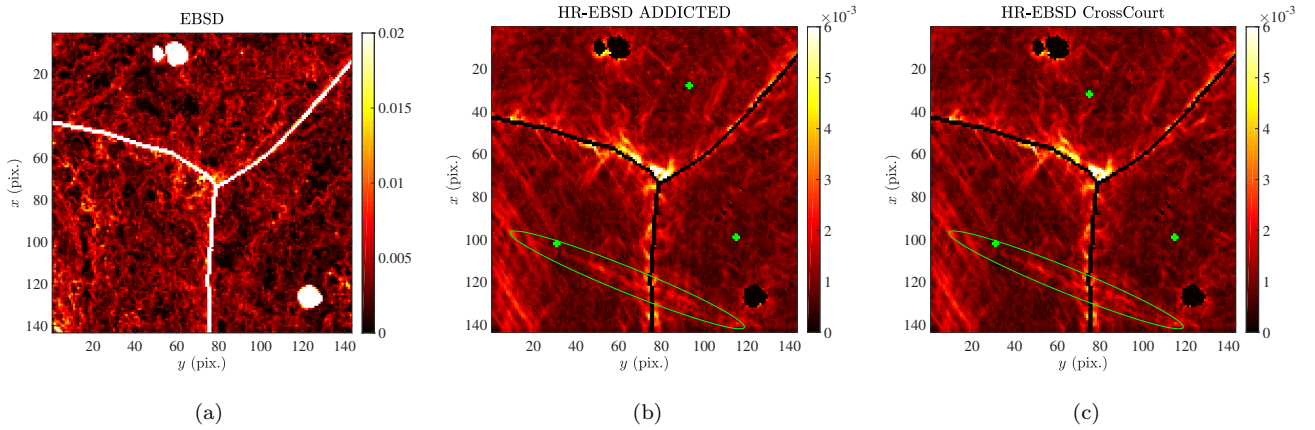


Figure 12: Kernel average misorientation obtained by (a) standard EBSD analyses, (b) ADDICTED (HR-EBSD), and (c) CrossCourt. The green crosses indicate the position of the reference diffraction images for each grain. The ellipses highlight inter-granular straight traces due to polishing artifacts/scratches.

Figure 13 further cross-validates the performance of CrossCourt and ADDICTED. As a measure of correlation quality, the (geometric mean over all ZOIs of) normalized XCF peak provided by CrossCourt is reported in Figure 13(a). It is found that this quantity is generally greater than 0.85, and the value is lower without remapping, thereby proving the beneficial effect of remapping. The quality factor map given by ADDICTED is shown in Figure 13(b). It is worth noting that Figures 13(a) and Figure 13(b) display values of different nature, thus they cannot be quantitatively compared to each other. However, higher values in Figures 13(a) and 13(b) both indicate better registration. The revealed trends are not exactly the same in Figures 13(a) and 13(b). The rotation maps obtained by the two methods with respect to the reference point chosen in each grain are shown in Figure 13(c) and 13(d). The rotation fields captured by the two methods are very close, except for the upper grain due to their different reference points. As a result, Figure 13 shows again that the data set was successfully processed by both softwares.

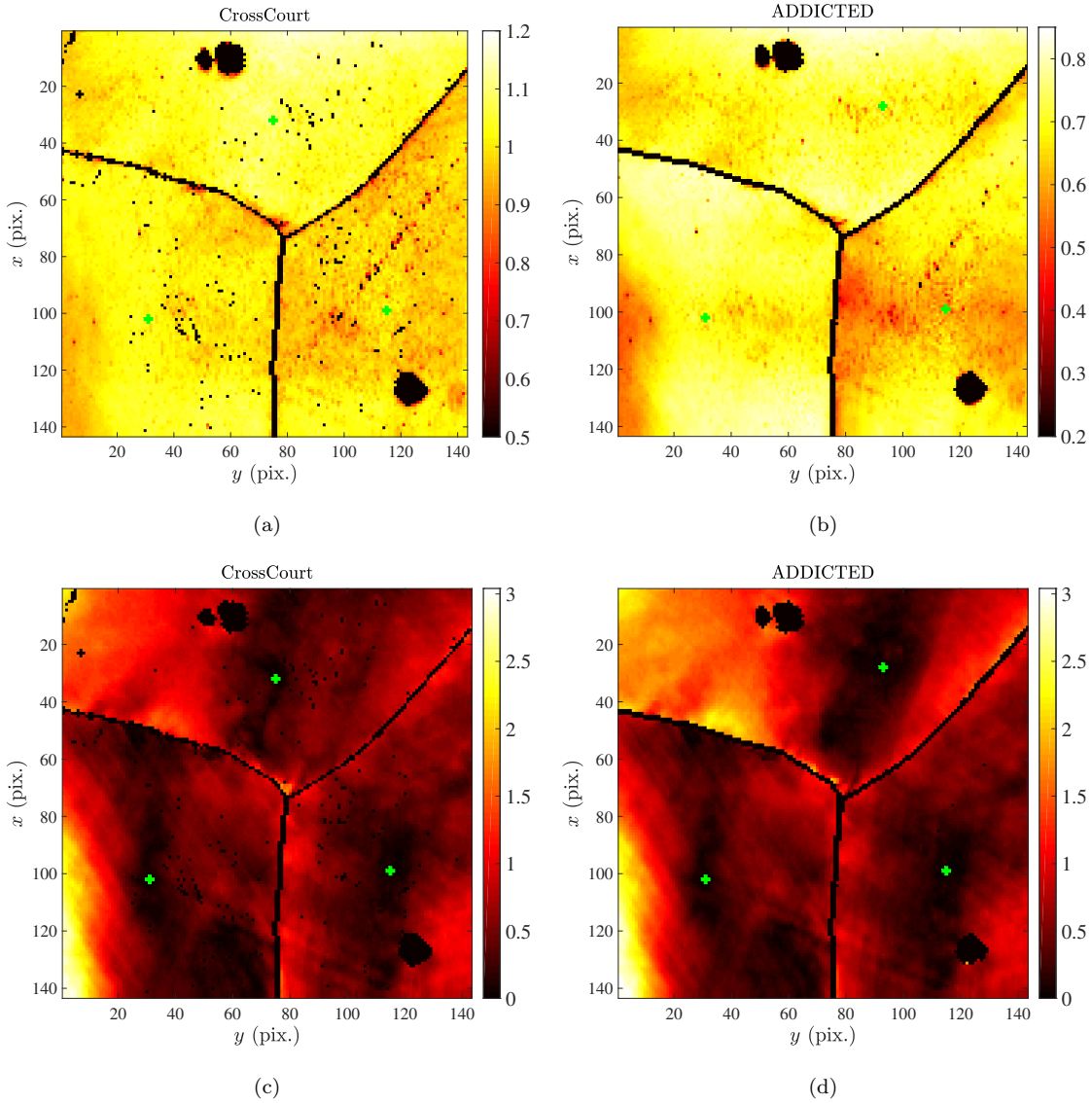


Figure 13: (a) Normalized XCF peak (geometrically averaged over all ZOIs) given by CrossCourt with remapping; (b) Quality factor of ADDICTED calculation; Relative rotation (expressed in degrees) obtained by CrossCourt with remapping (c) and ADDICTED (d). The green crosses indicate the position of the reference diffraction images for each grain. Note that they differ for the top grain.

In the elastic regime, the complete stress tensor is calculated by Hooke's law [8]

$$\boldsymbol{\sigma} = J^{-1} \mathbf{F}^e \mathcal{C} : \boldsymbol{\epsilon}(\mathbf{F}^e)^\top \quad (24)$$

where $\mathcal{C} : \boldsymbol{\epsilon}$ provides the stress tensor in the frame of the undeformed crystal (*i.e.*, second Piola-Kirchhoff tensor), and J the determinant of \mathbf{F}^e . The elastic constants $C_{11} = 206$ GPa, $C_{12} = 133$ GPa, $C_{44} = 119$ GPa are chosen for the two algorithms [37].

The stress components obtained by CrossCourt are presented in Figure 14 and those obtained by ADDICTED in Figure 15. The component σ_{zz} is by construction null and thus not presented. It is found that ADDICTED results in stress fields are more homogeneous than those of CrossCourt. Although measured stresses are only related

to those of the chosen reference point in each grain, and hence cannot strictly be considered as “absolute,” it is gratifying to observe that stress discontinuities at grain boundaries, and shear stresses at the free surface σ_{iz} are lower with ADDICTED although no such conditions have been enforced. Let us add that surprisingly, the effect of remapping in CrossCourt leads to an increase in the estimated stress level. A contact with the authors of this software did not elucidate the reasons for this effect. However, even without remapping, the stress magnitude obtained with CrossCourt is much higher than with ADDICTED.

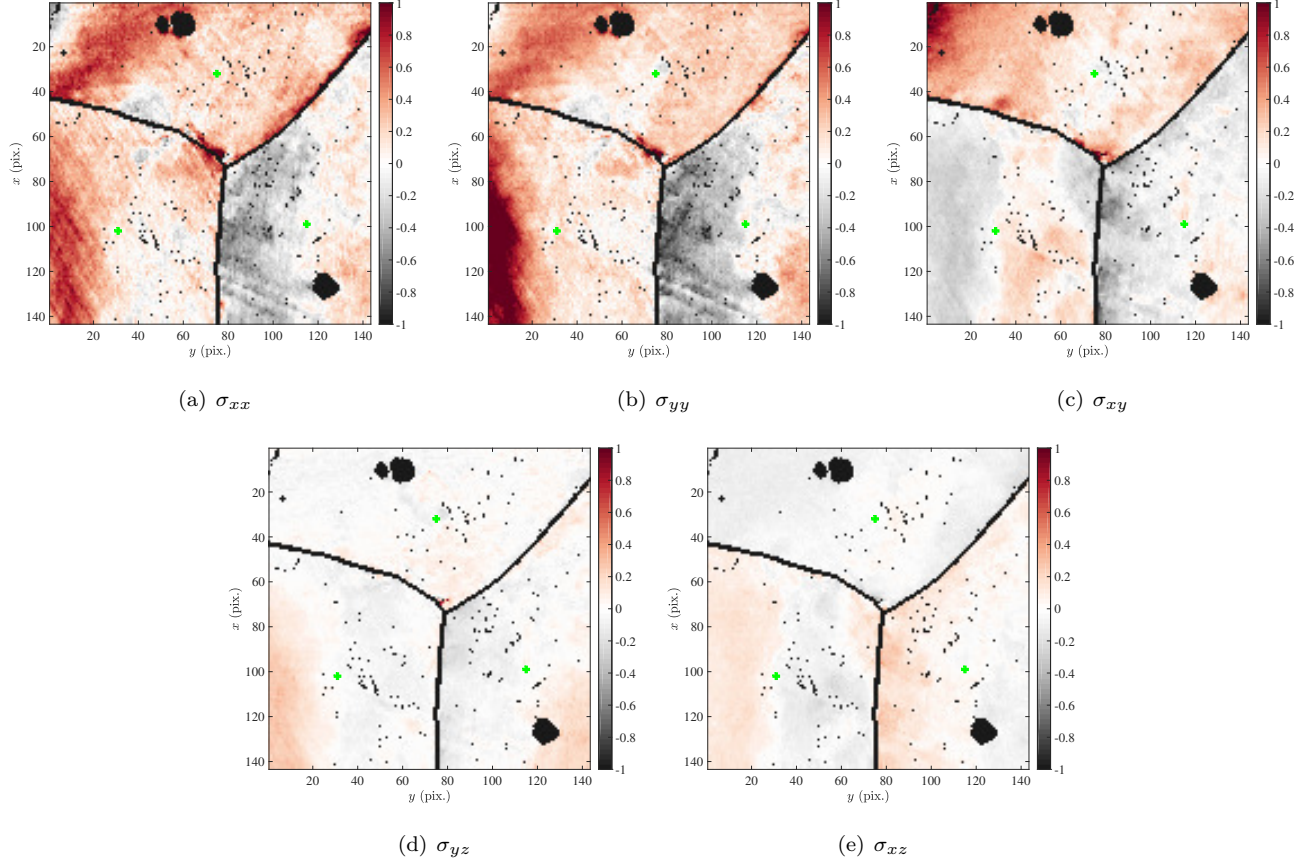


Figure 14: Stress tensor components (expressed in GPa) obtained by CrossCourt with application of remapping. (a) σ_{xx} , (b) σ_{yy} , (c) σ_{xy} , (d) σ_{yz} , (e) σ_{xz} . The component σ_{zz} is set to 0 (plane stress hypothesis), thus not shown. The green crosses indicate the position of the reference diffraction images.

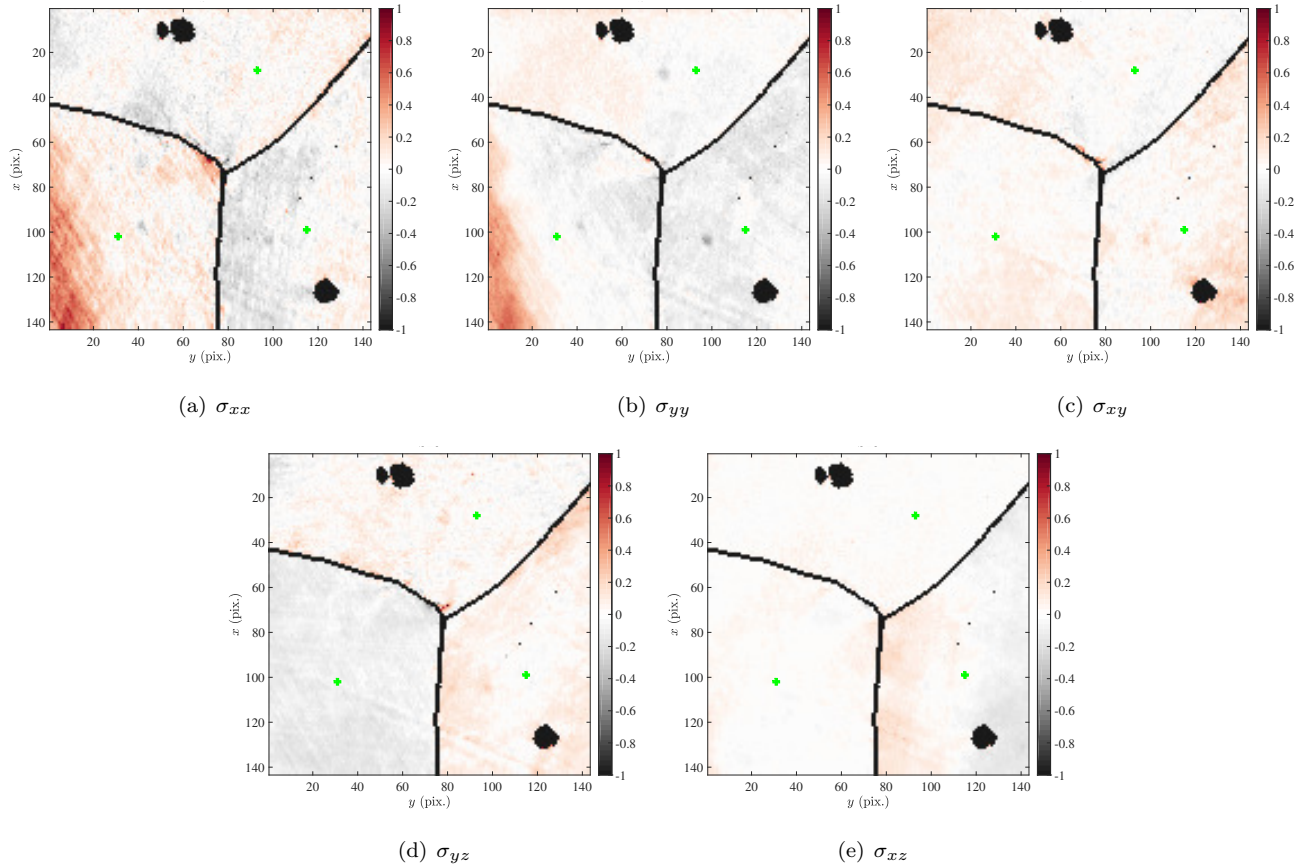


Figure 15: Stress tensor components (expressed in GPa) obtained by ADDICTED. (a) σ_{xx} , (b) σ_{yy} , (c) σ_{xy} , (d) σ_{yz} , (e) σ_{xz} . The component σ_{zz} is set to 0 (plane stress hypothesis), thus not shown. The green crosses indicate the position of the reference diffraction images for each grain.

Von Mises equivalent stresses are compared for ADDICTED and CrossCourt in Figure 16. It is concluded that the Von Mises stress field is more homogeneous and its level is lower with ADDICTED. The straight inter-granular line is always visible in the results provided by ADDICTED, contrary to those with cross-correlation, as highlighted by ellipses in Figures 16(a) and 16(b). It is noteworthy that this straight inter-granular line corresponds to a scratch that goes together with a residual stress signature, so that the mark is physical and not an artifact. It is therefore believed that ADDICTED captures the stress level precisely. The comparison of histograms of Figure 16(c) and 16(d) indicates that the high equivalent stresses obtained by CrossCourt (*i.e.*, greater than 0.6 GPa) disappear with the present approach. These unrealistic stress levels are significantly reduced.

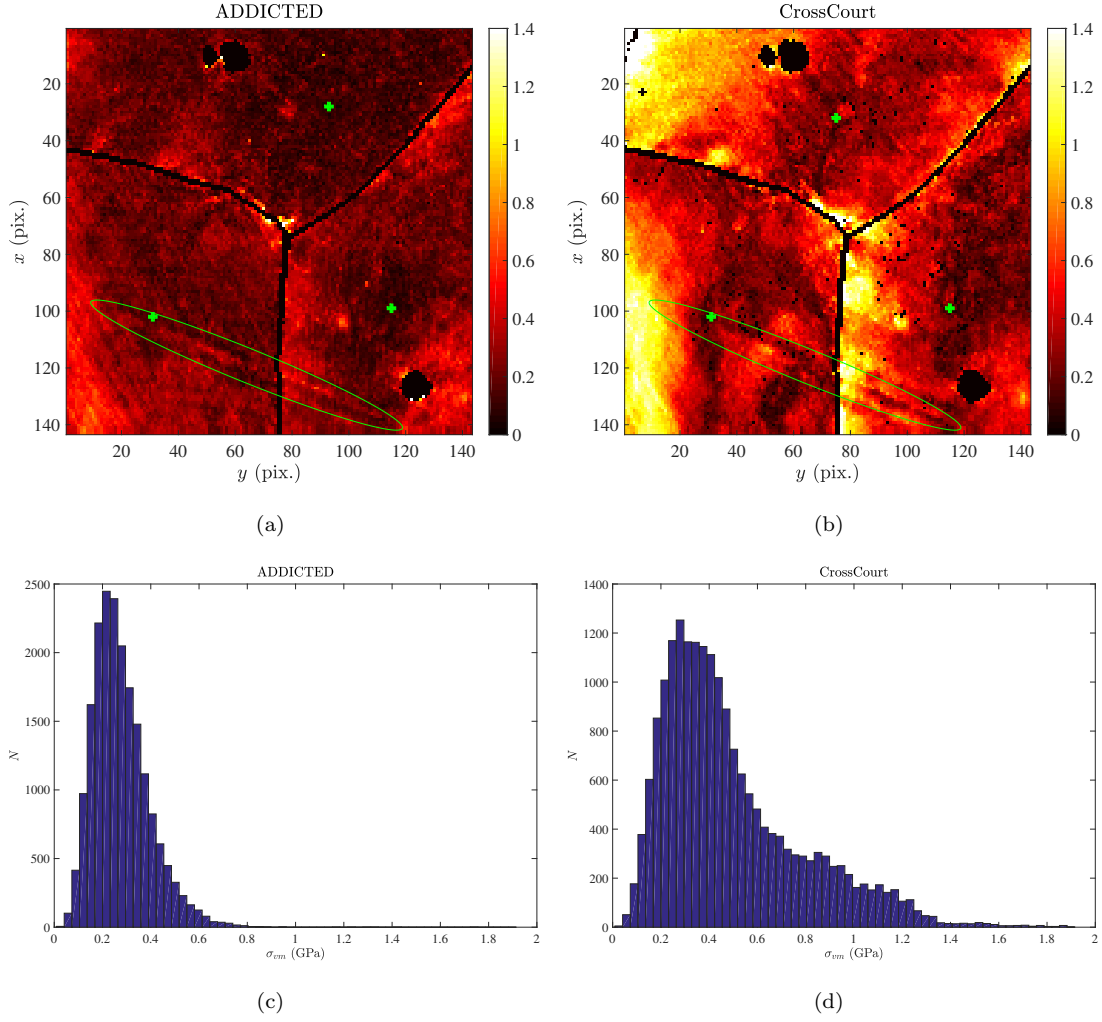


Figure 16: Von Mises equivalent stress (expressed in GPa) obtained by (a) ADDICTED and (b) CrossCourt softwares. The green crosses indicate the position of the reference diffraction images for each grain. The ellipses highlight inter-granular straight traces due to polishing artifacts/scratches, which are clearer in sub-figure (a) than (b). (c) and (d) are the histograms of sub-figures (a) and (b), respectively.

Another key point concerns the extreme value of Von Mises stress, which is equal to 6.5 GPa for CrossCourt, and 2.7 GPa for ADDICTED. It has been checked that for the two computations, the maximum values were reached for the same location, and hence for the same diffraction image. A lower equivalent stress also proves that this degraded image is more faithfully analyzed by ADDICTED.

In terms of computation time, ADDICTED takes 40 h on an HP laptop using *two* i7 cores. On a desktop machine running *eight* i7 cores, CrossCourt takes about 40 h for the first rough cross-correlation, and 100 hours with the second cross-correlation “*after remapping*”. The fact that the present algorithm drastically reduces (by about 75% compared to cross-correlation “*without remapping*”, or about 90% compared to cross-correlation “*with remapping*”) the computation time with an interpreted language is very encouraging for generalizing and extending the technique to industrial applications.

Although the user manual of CrossCourt suggests that more ZOIs should be taken in case of high rotation,

and currently 96 ZOIs were taken, this number can be reduced by a factor of 4 (leading to a similar saving in computation time) without any significant change in the quality of the result. When such a reduction is used, the benefit of using ADDICTED as compared to CrossCourt with remapping is still a gain of 60% in computation time. However, the question of finding the appropriate number of ZOIs remains open.

5 Conclusion

This paper has revisited the main ideas exploited in HR-EBSD and developed in the last decade in order to measure elastic strains and estimate stresses. To process diffraction images, instead of cross-correlating image subsets, integrated DIC was employed over the quasi-totality of the image constructed directly with the most appropriate formulation of the problem, namely, the geometrical projection equations of diffraction patterns onto the detector plane, in a similar spirit as the algorithm proposed in Ref. [19].

The so-called ADDICTED algorithm has the following advantages:

1. Simple implementation. The pre-rotation step (*i.e.*, “remapping”) is intrinsically incorporated in ADDICTED.
2. Robustness of calculation, since the 8 components of the deformation gradient tensor are directly computed by analyzing only once the whole diffraction image. This property has been checked on degraded EBSPs. The exploitation of the studied images is complete and does not introduce spatial correlations between neighboring calculation points.
3. The strategy of global correlation reduces the measurement uncertainty. For example in the test case on a slightly deformed single crystal sample, by using the same reference EBSP and excluding points at activated slip lines, the strain measurement uncertainty is 3.6×10^{-5} for ADDICTED and 4.3×10^{-5} for local-DIC based HR-EBSD technique. In the optimal conditions, the measurement uncertainty has been reduced to 2.8×10^{-5} . The algorithm takes a large and unique ROI, *i.e.*, it samples once and for all large quantities of data. By drastically reducing the sampling bias of cross-correlation, ADDICTED is optimal in terms of least sensitivity to white Gaussian noise corrupting diffraction images.
4. Global correlation also allows redundant calculations to be avoided, which is largely present with the cross-correlation method due to large overlapping subsets. As a result, ADDICTED is considerably less costly in computation time (60% according to the test case).
5. Optimizations of the ADDICTED computation have been proposed (*e.g.*, Gaussian filtering on diffraction images to mitigate high frequency noise, initialization of ADDICTED computations by the results of neighboring pixels).
6. The residual field of the correlation technique is intrinsically obtained by integrated DIC, while it is not naturally calculated by cross-correlation approaches. The residual field is a good indicator of the computation performance. The information contained in the residual maps can be exploited in different ways, and this paper provides few examples. For example, residual fields reveal the shortcomings of the HR-EBSD transformation model at activated slip systems (Figure 6(b)). By using residual maps of numerous calculations, EBSPs can

be denoised (Figure 8(c)). The unreliable pixels of the EBSD detector are easily identified and located by analyzing numerous residual maps. Possible errors in the image background corresponding to EBSPs were also detected (Figure 11(h)).

Last, ADDICTED, which is adapted to HR-EBSD images, could be extended to several other types of diffraction images (*e.g.*, Kossel, Laue, or TEM diffraction). These techniques derive from the same principles of projection of diffracted beams and after a simple modification, ADDICTED could be applied to those images as well. Integrated algorithms for Laue and TEM diffraction, with all the above cited advantages, would bring significant gains to their exploitations.

Acknowledgments

The authors acknowledge the financial support of Euratom research and training program 2014-2018 SOTERIA under grant agreement No. 661913. This paper reflects only the authors' view and that the Commission is not responsible for any use that may be made of the information it contains. They also thank Dr. Emeric Plancher, Mr. Dominique Loisonard, Dr. Julien Stodolna and Dr. Claire Maurice for providing their experimental data and constructive advices.

Appendix A: Geometric basis of HR-EBSD

This presentation of the geometric basis of HR-EBSD can be found more detailed in Refs. [10, 38]. The principle is recalled hereafter for defining the notations. Let \mathbf{F} define the deformation gradient tensor that, when applied to a current point \mathbf{X} in the initial configuration of the reference crystal, allows its position \mathbf{x} in the deformed configuration to be obtained

$$\mathbf{F} = \frac{d\mathbf{x}}{d\mathbf{X}} = \begin{bmatrix} \frac{\partial x}{\partial X} & \frac{\partial x}{\partial Y} & \frac{\partial x}{\partial Z} \\ \frac{\partial Y}{\partial X} & \frac{\partial Y}{\partial Y} & \frac{\partial Y}{\partial Z} \\ \frac{\partial Z}{\partial X} & \frac{\partial Z}{\partial Y} & \frac{\partial Z}{\partial Z} \end{bmatrix} \quad (25)$$

\mathbf{F} can be decomposed into two parts, namely, the elastic \mathbf{F}^e and plastic \mathbf{F}^p parts

$$\mathbf{F} = \mathbf{F}^e \mathbf{F}^p \quad (26)$$

The effects of plastic strains and volumetric elastic strains are summarized in Ref. [8]. Plastic strains, more precisely dislocations and resulting severe but local strain gradients, make the Kikuchi bands less sharp and contrasted, an effect that is difficult to quantify. Thus HR-EBSD does not allow the plastic strains to be measured. In case of volumetric elastic strains, a variation of Kikuchi band width is observed. This width variation is not well resolved in HR-EBSD techniques and this hydrostatic (or spherical) elastic strain component will not be considered as measurable and thus not exploited in the sequel [6]. Conversely, the deviatoric elastic strain tensor modifies the shape of the crystalline lattice, *i.e.*, the relative orientation of the crystalline planes, thus the diffracted electron patterns. A projection onto a screen far from the diffraction source amplifies the angular distances between the two beams, thus generates a measurable variation between diffraction images.

Since only eight components of \mathbf{F}^e are measurable, a convention should be made to set the lacking degree of freedom. Here the tensor $\widehat{\mathbf{F}}^e$ is chosen such that its ninth component is set to 1

$$\widehat{\mathbf{F}}^e = \begin{bmatrix} \hat{F}_1^e & \hat{F}_2^e & \hat{F}_3^e \\ \hat{F}_4^e & \hat{F}_5^e & \hat{F}_6^e \\ \hat{F}_7^e & \hat{F}_8^e & 1 \end{bmatrix} \quad (27)$$

The real elastic deformation gradient tensor \mathbf{F}^e reads

$$\mathbf{F}^e = \left(\frac{\partial z}{\partial Z} \right) \widehat{\mathbf{F}}^e \quad (28)$$

The factor $\partial z/\partial Z$ is not measurable, but can be determined by additional hypotheses such as the commonly adopted plane stress hypothesis of the studied zone [14]. The plane stress hypothesis has been proven “admirably robust” in HR-EBSD analyses, except when sampling very close to localized stress field sources [39].

The fundamental equation of HR-EBSD describes the projection of the diffraction cones onto the detector plane. This projection is illustrated in Figure 17. The detector defines the coordinate system with its lower left corner as the origin. An electron beam hits the sample with an inclination of typically 70° with respect to the normal direction. A “central” point of the interaction zone is considered as the “effective” source of the diffracted electrons (different from the incident beam), which is represented by S . The “projection center” O is the normal projection of S onto the detector plane. Its coordinates are denoted as $(x^*, y^*, 0)$. Let z^* be the distance between S and O . Thus S has coordinates $(x^*, y^*, -z^*)$.

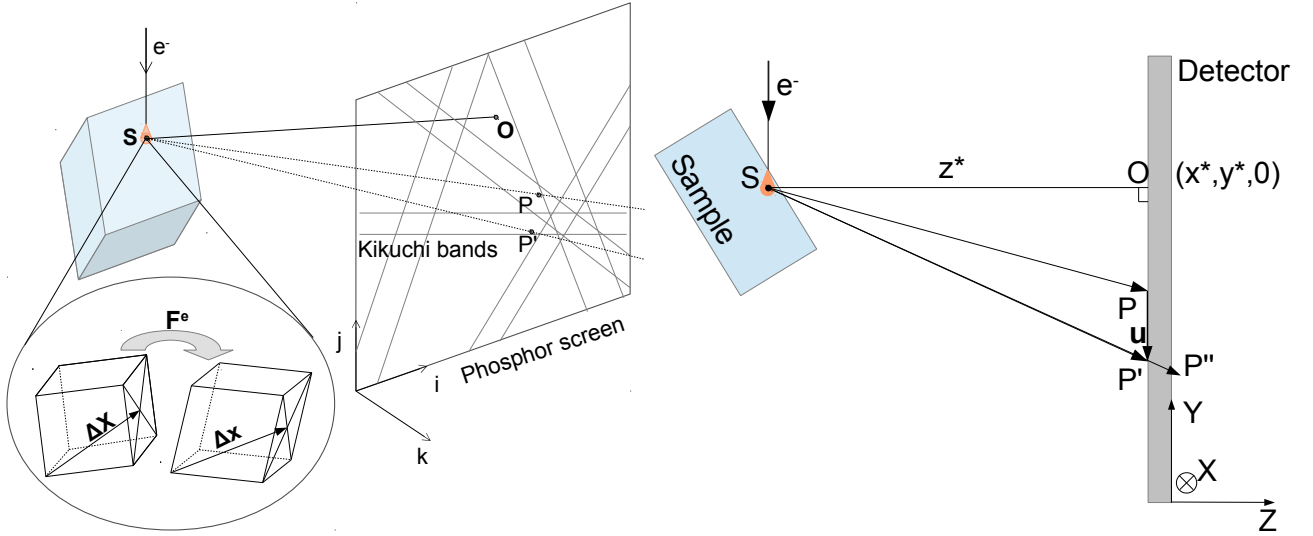


Figure 17: Sketch illustrating the geometry of HR-EBSD in 3D (a), adapted from Ref. [10], and in 2D (b).

Let us consider an element $\Delta\mathbf{X}$ in the reference crystal lattice, and assume this particular direction generates a diffracted beam that intersects the detector plane at point P , of coordinates $(x, y, 0)$. In the following, the vector \mathbf{SP} is denoted as \mathbf{p} . Then $\{\mathbf{p}\} = \{\Delta x, \Delta y, \Delta z\}^\top = \{x - x^*, y - y^*, z^*\}^\top = \alpha\Delta\mathbf{X}$, where α is the projection scale.

If the interaction volume around the source point S is subjected to an elastic deformation described by the deformation gradient tensor \mathbf{F}^e , *i.e.*, then the reference element $\Delta\mathbf{X}$ is transformed into $\Delta\mathbf{x} = \mathbf{F}^e\Delta\mathbf{X}$. The

diffracted beam, which was initially along direction \mathbf{p} , has now moved to point P'' , so that

$$\mathbf{p}'' = \alpha \mathbf{F}^e \Delta \mathbf{X} \quad (29)$$

where vector \mathbf{SP}'' is denoted as \mathbf{p}'' . The straight line SP'' intersects the detector plane at point P' [38]. The apparent motion on the detector plane is $\mathbf{u} = \mathbf{p}' - \mathbf{p}$ (*i.e.*, vector \mathbf{PP}')

$$\begin{aligned} \mathbf{u} &= \mathbf{p}' - \mathbf{p} \\ &= \frac{z^*}{(\widehat{\mathbf{F}}^e \cdot \mathbf{p})_z} \widehat{\mathbf{F}}^e \cdot \mathbf{p} - \mathbf{p}, \end{aligned} \quad (30)$$

or in an explicit form, for pixel (x, y) of the detector,

$$\begin{aligned} u_x(x, y) &= \frac{z^*(\widehat{F}_1^e(x - x^*) + \widehat{F}_2^e(y - y^*) + \widehat{F}_3^e z^*)}{\widehat{F}_7^e(x - x^*) + \widehat{F}_8^e(y - y^*) + z^*} - (x - x^*) \\ u_y(x, y) &= \frac{z^*(\widehat{F}_4^e(x - x^*) + \widehat{F}_5^e(y - y^*) + \widehat{F}_6^e z^*)}{\widehat{F}_7^e(x - x^*) + \widehat{F}_8^e(y - y^*) + z^*} - (y - y^*) \end{aligned} \quad (31)$$

To summarize, the displacement field (u_x, u_y) between a reference diffraction image and a diffraction image of the deformed configuration reflects the elastic strains of the crystal lattice at the studied point with respect to the chosen reference crystal. The determination of tensor $\widehat{\mathbf{F}}^e$ is the major objective of HR-EBSD.

Appendix B: Single crystal sample in 4-point flexural test

A 4-point flexural test has been performed by Plancher et al. on a Zeiss Supra 55VP FEG-SEM operating at 20 kV with a probe current of 2.4 nA [8, 15]. A sample made of A316 stainless steel has been obtained by electric arc erosion from a single crystal ingot. The sample is oriented along the $\langle 100 \rangle$ axis with an uncertainty of 3° . Then the sample has been mechanically and electrochemically polished to minimize the surface residual stress. The final sample is of dimensions $30 \times 4.8 \times 0.5$ mm³. It was tested by a 4-point flexural setup, which is illustrated in Figure 18. During the test the maximum force reached 5.4 N. A transverse profile has been studied to get its strain state, which is representative of the loading of the central part of the sample. Along this 500 μ m long profile, HR-EBSD acquisitions have been performed over 5000 points, with a step size of 100 nm. The diffraction images have been recorded by a Nordlys II camera with a definition of 1344×1024 pixels. The sample has also been studied by synchrotron X-ray diffraction, in order to apply the DIC-Laue technique [40]. The Laue diffraction technique provides a comparison of coarser resolution, because the focused synchrotron beam has a diameter larger than the electron beam of SEMs. However, the Laue diffraction combined with DIC leads to a lower uncertainty on the (elastic) strain measurements (of the order of 10^{-5}) due to an averaging effect as it is less local than HR-EBSD [15].

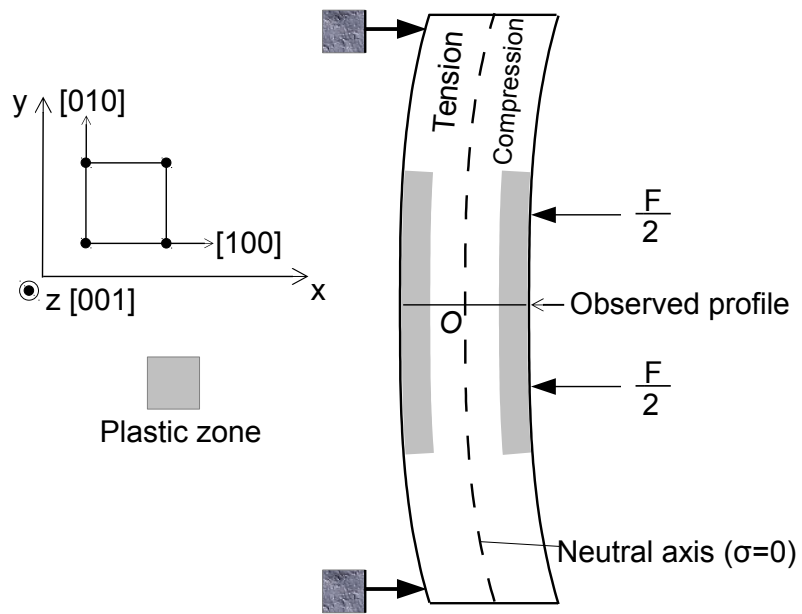


Figure 18: Sketch of 4-point flexural test [15].

References

- [1] L. Li and M. Han. Determining the Bravais lattice using a single electron backscatter diffraction pattern. *Journal of Applied Crystallography*, 48(1):107–115, 2015.
- [2] F. Ram, S. Zaefferer, T. Jäpel, and D. Raabe. Error analysis of the crystal orientations and disorientations obtained by the classical electron backscatter diffraction technique. *Journal of Applied Crystallography*, 48(3):797–813, 2015.
- [3] Q. Shi, F. Latourte, F. Hild, and S. Roux. Quaternion correlation for tracking crystal motions. *Measurement Science and Technology*, 27(9):095006, 2016.
- [4] J. Jiang, T.B. Britton, and A.J. Wilkinson. Measurement of geometrically necessary dislocation density with high resolution electron backscatter diffraction: Effects of detector binning and step size. *Ultramicroscopy*, 125:1–9, 2013.
- [5] T.B. Britton, J. Jiang, R. Clough, E. Tarleton, A.I. Kirkland, and A.J. Wilkinson. Assessing the precision of strain measurements using electron backscatter diffraction - part 1: Detector assessment. *Ultramicroscopy*, 135:126 – 135, 2013.
- [6] A.J. Wilkinson, G. Meaden, and D.J. Dingley. High-resolution elastic strain measurement from electron backscatter diffraction patterns: New levels of sensitivity. *Ultramicroscopy*, 106(4-5):307 – 313, 2006.
- [7] A. J. Wilkinson and T. B. Britton. Strains, planes, and EBSD in materials science. *Materials Today*, 15:366–376, 2012.
- [8] E. Plancher. *Full-field measurements of elastic and total strains for the determination of the local behaviour in polycrystals*. PhD thesis, Ecole nationale supérieure d’arts et métiers - ENSAM, December 2015.
- [9] G. Miyamoto, A. Shibata, T. Maki, and T. Furuhashi. Precise measurement of strain accommodation in austenite matrix surrounding martensite in ferrous alloys by electron backscatter diffraction analysis. *Acta Materialia*, 57(4):1120 – 1131, 2009.
- [10] C. Maurice, J. Driver, and R. Fortunier. On solving the orientation gradient dependency of high angular resolution EBSD. *Ultramicroscopy*, 113:171–181, November 2012.
- [11] T.B. Britton and A.J. Wilkinson. High resolution electron backscatter diffraction measurements of elastic strain variations in the presence of larger lattice rotations. *Ultramicroscopy*, 114:82 – 95, 2012.
- [12] T.B. Britton and J.L.R. Hickey. Understanding deformation with high angular resolution electron backscatter diffraction (HR-EBSD). *IOP Conference Proceedings Proceedings of EMAS-2017/IUMAS-7*, 2017.
- [13] A.J. Wilkinson and D. Randman. Determination of elastic strain fields and geometrically necessary dislocation distributions near nanoindentations using electron back scatter diffraction. *Philosophical Magazine*, 90(9):1159–1177, 2010.

- [14] AJ Wilkinson, G Meaden, and DJ Dingley. High resolution mapping of strains and rotations using electron backscatter diffraction. *Materials Science and Technology*, 22(11):1271–1278, 2006.
- [15] E. Plancher, J. Petit, C. Maurice, V. Favier, L. Saintoyant, D. Loinsard, N. Rupin, J.-B. Marijon, O. Ulrich, M. Bornert, J.-S. Micha, O. Robach, and O. Castelnau. On the accuracy of elastic strain field measurements by Laue microdiffraction and high-resolution EBSD: a cross-validation experiment. *Experimental Mechanics*, 56(3):483–492, 2016.
- [16] T. Zhang, D.M. Collins, F.P.E. Dunne, and B.A. Shollock. Crystal plasticity and high-resolution electron backscatter diffraction analysis of full-field polycrystal Ni superalloy strains and rotations under thermal loading. *Acta Materialia*, 80(Supplement C):25 – 38, 2014.
- [17] CrossCourt4. www.blgproductions.co.uk. BLG Productions Ltd, Bristol, UK, 2016.
- [18] S. Villert. *Analyse des déformations élastiques locales par la technique EBSD*. PhD thesis, 2008. Ecole des Mines Saint-Etienne.
- [19] T. Vermeij and J.P.M. Hoefnagels. A consistent full-field integrated DIC framework for HR-EBSD. *Ultramicroscopy*, 2018.
- [20] Q. Shi. *Experimental and numerical studies on the micromechanical crystal plasticity behavior of an RPV steel*. PhD thesis, University of Paris-Saclay, April 2018.
- [21] B. Wagne, S. Roux, and F. Hild. Spectral approach to displacement evaluation from image analysis. *European Physical Journal: Applied Physics*, 17:247–252, 2002.
- [22] G. Besnard, F. Hild, and S. Roux. "Finite-Element" displacement fields analysis from digital images: application to Portevin-Le Châtelier bands. *Experimental Mechanics*, 46:789–803, 2006.
- [23] F. Hild and S. Roux. Digital image correlation: from displacement measurement to identification of elastic properties - a review. *Strain*, 42(2):69–80, 2006.
- [24] S. Roux and F. Hild. Stress intensity factor measurements from digital image correlation: post-processing and integrated approaches. *International Journal of Fracture*, 140(1):141–157, 2006.
- [25] H. Leclerc, J.-N. Périé, S. Roux, and F. Hild. Integrated digital image correlation for the identification of mechanical properties. *MIRAGE 2009, LNCS*, 5496:161–171, 2009.
- [26] C. Maurice. Recent advances in HR-EBSD: Overcoming current limitations. In *HR-EBSD Workshop – London*, 2014.
- [27] F. Hild and S. Roux. Comparison of local and global approaches to digital image correlation. *Experimental Mechanics*, 52:1503–1519, 2012.
- [28] BLG PRODUCTIONS LTD. Methods, apparatuses and computer programs for crystallography, october 2012.

- [29] S.I. Wright. Fundamentals of automated EBSD. In Adam J. Schwartz, Mukul Kumar, and Brent L. Adams, editors, *Electron Backscatter Diffraction in Materials Science*, pages 51–64. Springer US, Boston, MA, 2000.
- [30] D.J. Dingley, S.I. Wright, and M.W. Nowell. Dynamic background correction of electron backscatter diffraction patterns. *Microscopy and Microanalysis*, 11(S02):528, 2005.
- [31] C. Maurice, R. Fortunier, J. Driver, A. Day, K. Mingard, and G. Meaden. Comments on the paper "Bragg's law diffraction simulations for electron backscatter diffraction analysis" by Josh Kacher, Colin Landon, Brent L. Adams and David Fullwood. *Ultramicroscopy*, 110(7):758 – 759, 2010.
- [32] F. Hild and S. Roux. Digital image correlation. In P. Rastogi and E. Hack, editors, *Optical Methods for Solid Mechanics. A Full-Field Approach*, pages 183–228. Wiley-VCH, Weinheim (Germany), 2012.
- [33] V. Tong, J. Jiang, A. J. Wilkinson, and T. B. Britton. The effect of pattern overlap on the accuracy of high resolution electron backscatter diffraction measurements. *Ultramicroscopy*, 155(Supplement C):62 – 73, 2015.
- [34] Q. Shi, S. Roux, F. Latourte, F. Hild, D. Loisonard, and N. Brynaert. Measuring topographies from conventional SEM acquisitions. *Ultramicroscopy*, 191:18 – 33, 2018.
- [35] J.F. Nye. Some geometrical relations in dislocated crystals. *Acta Metallurgica*, 1:153–162, 1953.
- [36] D. Caillard. Dislocation-obstacle interactions and mechanical properties of intermetallics. *Journal de Physique IV Colloque*, 06:199–210, 1996.
- [37] H.M. Ledbetter. Predicted single-crystal elastic constants of stainless-steel 316. *British Journal of Non-Destructive Testing*, 23:286–287, 1981.
- [38] C. Maurice, R. Quey, R. Fortunier, and J.H. Driver. High angular resolution EBSD and its materials applications. In *Microstructural Design of Advanced Engineering Materials*, pages 339–365. Wiley-VCH Verlag GmbH & Co. KGaA, 2013.
- [39] T.J. Hardin, T.J. Ruggles, D.P. Kock, S.R. Niezgoda, D.T. Fullwood, and E.R. Homer. Analysis of traction-free assumption in high-resolution EBSD measurements. *Journal of Microscopy*, 260(1):73–85, 2015.
- [40] J. Petit, O. Castelnau, M. Bornert, F. G. Zhang, F. Hofmann, A. M. Korsunsky, D. Faurie, C. Le Bourlot, J. S. Micha, O. Robach, and O. Ulrich. Laue-DIC: a new method for improved stress field measurements at the micrometer scale. *Journal of Synchrotron Radiation*, 22(4):980–994, 2015.